OCCURRENCE PATTERNS OF WHISTLER MODE (WM) ECHOES OBSERVED BY RPI/IMAGE AND THEIR RELATION TO GEOMAGNETIC ACTIVITY

By

Amani Reddy

RECOMMENDED:

Advisory Committee Chair

Chair, Department of Electrical and Computer Engineering

APPROVED:

Dean, College of Engineering and Mines

Dean of the Graduate School

Nov 30, 2007

Date

OCCURRENCE PATTERNS OF WHISTLER MODE (WM) ECHOES OBSERVED BY RPI/IMAGE AND THEIR RELATION TO GEOMAGNETIC ACTIVITY

A

THESIS

Presented to the Faculty

of the University of Alaska Fairbanks

in Partial Fulfillment of the Requirements

for the Degree of

MASTER OF SCIENCE

By

Amani Reddy, B.Tech.

Fairbanks, Alaska

December 2007

Abstract

This thesis presents an analysis of whistler mode (WM) echoes observed at altitudes less than 5,000 km by the Radio Plasma Imager (RPI) on the IMAGE satellite. WM echoes are generated either by specular reflection (SR) of RPI signals at the Earth-ionosphere boundary (~90 km) or by magnetospheric reflection of RPI signals (lower hybrid frequency, $f_{lh} \gtrsim$ wave frequency, f) at altitudes greater than 1,000 km [Sonwalkar et al., 2004; Sonwalkar et al., 2006]. These echoes are further influenced by field aligned irregularities (FAI) and are categorized into discrete, multipath or diffuse SR- and MR-WM echoes, based on their characteristic spectral forms. A survey of WM echoes observed during January 2004- December 2005 showed that WM echoes occurred at all latitudes and under moderate geomagnetic conditions. Occurrence patterns of WM echoes observed in August-December 2005 during geomagnetically quiet and disturbed periods indicate that geomagnetic storms lead to significant changes in FAI that affect the propagation of WM echoes. Our results help (1) in better understanding propagation and generation mechanisms of naturally occurring WM waves, and (2) in planning future WM wave injection experiments in space.

Table of Contents

Page

Page

List of Figures

Page

Page

Page

Page

Acknowledgements

I am sincerely grateful to my advisor Dr. Vikas Sonwalkar for his continuous support, encouragement, timely suggestions, active criticism, and the trust he placed in me. It has been a great learning experience working under his guidance. I learnt a great deal of data processing from him. He taught me how to break complex problems into simpler forms. I would like to thank Dr. William A. Bristow and Dr. Joseph G. Hawkins for sharing their views as committee members and taking time to read my thesis in the midst of their busy schedule.

I would like to thank my colleagues Radha Krishna Proddaturi for helping me with various aspects of RPI/IMAGE data and introducing me to ray tracing program, Arun Venkatasubramanian, for his timely suggestions and help with LATEX, and Blake S. Rider, for taking time to read my thesis and helping with data downloading.

This thesis could not have been accomplished without the constant support, encouragement, and understanding from my family. I would like to thank my dad, Veera Reddy, who will always be my role model, my ever loving mom, Kavitha Reddy, who always encourages me, and my brother, Anvesh Reddy, who stood by me all the time. I greatly appreciate their trust, support and willingness to give me space to develop and finish my thesis.

I have been fortunate to have wonderful friends in my life who keep a smile on my face no matter what the circumstance. I would like to specially thank Venkatramana Reddy Revuri, for his words of encouragement and advise, as he stood by me during the tiring times of research. I would like to thank Bindu Madhavi Gadamsetty for bearing with my nervous tantrums and standing by me through tough times.

The research work resulting in my thesis at the University of Alaska Fairbanks was supported by NASA under contract NNG04GI67G. I would like to thank graduate school for supporting me through thesis completion fellowship in the final stages of my M.S. And I would also like to thank ECE department for offering me a teaching assistantship during the first two semesters of my Master's program.

Chapter 1 Introduction

1.1 Objectives of this thesis

This research concerns the study of whistler mode (WM) echoes observed by the radio plasma imager (RPI) on the IMAGE satellite to understand the low altitude region (<5,000 km) of the magnetosphere. The objective of the first part of this thesis is to present the occurrence pattern of WM echoes observed during the 2004 January-August 2005 period as a function of geophysical conditions (location, MLT, and geomagnetic activity). The objective of the second part of the thesis is to perform detailed case studies on the occurrence pattern of WM echoes during selected geomagnetically quiet and disturbed periods in August-December 2005 period.

1.2 Organization of this chapter

The first section of this chapter presents the objectives of this thesis. The second section presents the organization of this chapter. The third section describes the background and past work done related to this thesis work. The fourth section presents the significance of this thesis work. The fifth section discusses the problem statement and approach. The sixth section presents the contribution of this thesis work and the last section describes the organization of this thesis.

1.3 Background and past work

The Earth's upper atmosphere, comprising of Earth's ionosphere and magnetosphere, consists of cold and hot plasma, plasma waves, and geomagnetic field. The ionosphere begins at 70 km and extends up to 300 km. The magnetosphere extends upward from the ionosphere.

It extends outward from the Earth about 60,000 km toward the Sun and has a tail that extends many times that distance in the direction away from the Sun. The cold plasma consists mainly of electrons, H+, He+, and O+ ions. The inner magnetosphere, called plasmasphere, is a high density (100-1000 el/cc) cold plasma region that co-rotates with the Earth. The boundary of the plasmasphere is called plasmapause. The magnetosphere also contains two zones of energetic particles, called the Van Allen radiation belts [Sonwalkar, 2007]. The magnetosphere ends at a boundary known as the magnetopause, beyond which is the domain of the solar wind.

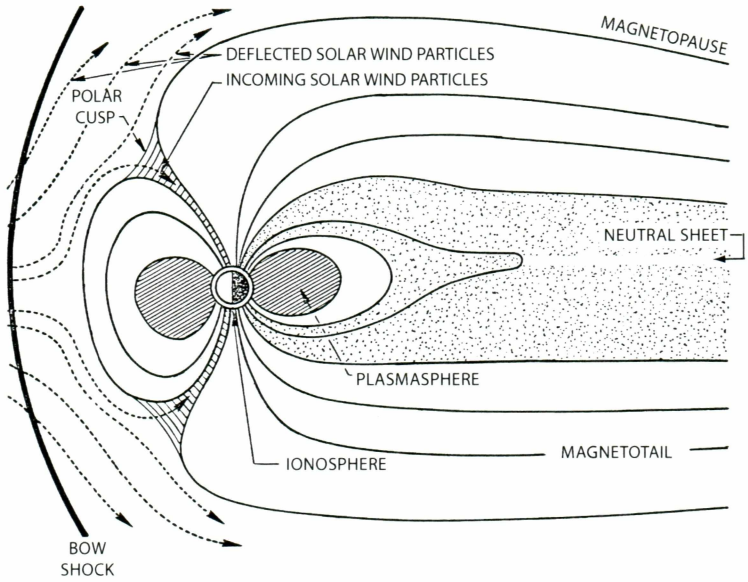

Figure 1.1. Schematic showing various regions of the Earth's magnetosphere. Adapted from *Sonwalkar* [2006]

The earth's magnetosphere supports a variety of cold plasma wave modes. Each mode is named depending on the properties of the waves (frequency, polarization, and refractive index) that propagate in that mode. Whistler mode (WM) waves propagate in the magnetosphere at a frequency (f) below either the electron plasma frequency (f_{pe}) or the electron gyro frequency (f_{ce}), whichever is lower. These waves are found in all parts of the magnetosphere. Because of their large refractive index that varies over three to four

orders of magnitude (∼1-10,000), slow phase and group velocities, and their accessibility to most parts of the magnetosphere, WM waves play an important role in the magnetospheric physics and have proved to be a powerful tool for magnetospheric cold and hot plasma diagnostics [Storey, 1953; Helliwell 1965; Carpenter, 1966; Helliwell, 1988; Sonwalkar et al., 1997; Carpenter et al., 1997]. The refractive index surfaces of WM waves are such that the ray propagation is mostly close to the magnetic field line (**B**), allowing remote sensing along the field line. WM echoes are generated either by the reflection of VLF waves at the Earth-Ionosphere boundary (∼90 km) or at altitudes where the local lower hybrid frequency (f_{lh}) is equal to the wave frequency (f). The former are called specularly reflected (SR) whistler mode (WM) echoes and the latter are called magnetospherically reflected (MR) whistler mode (WM) echoes.

WM waves are profoundly affected by plasma density structures of wide scale lengths (10 m - 100 km) present in the magnetosphere through the process of reflection, refraction, and scattering [Helliwell, 1965; James, 1972; Bell, 1983; Sonwalkar et al., 1984; Sonwalkar and Harikumar, 2000; Sonwalkar, 2006; and references therein]. Plasma density structures have an elongated shape along the geomagnetic field line (**B**) and are therefore called field aligned irregularities (FAI). FAIs are generated by various processes including plasma instabilities, particle precipitation, and plasma drifts occurring in the ionosphere [Kelley, 1989]. These plasma processes are enhanced during geomagnetically disturbed conditions, leading to the generation of plasma density structures. Study of FAIs is important because they contribute to the fading of high-frequency trans-ionospheric signals and to the degradation of ground-satellite communication. Thus, FAIs are one of the key indicators of space weather. Plasma density and density irregularities are also found to play an important role in many physical processes taking place at low and high latitudes such as wave particle interactions, mode conversion, particle precipitation and acceleration, auroral activity, and magnetic storm and substorm activity [Kelley, 1989; Schunk and Nagy, 2000; Sojka et al., 2000].

In the past, electron density (Ne) and density structures have been measured from top-side or bottomside sounding using radio waves in the high frequency (HF) range. Electron

density is also determined from in situ satellite measurements using plasma density probes [Kletzing et al.,1998]. Persoon et al. [1983] has shown that the upper cutoff frequency of auroral hiss gives the measurement of Ne. Given the gyro frequency, Ne can be calculated from the upper hybrid frequency (f_{uh}) measured from the slow Z-mode (ZM) band seen on dynamic spectra [Benson et al., 2003]. All these measurements are either limited to high altitudes (>5000 km) or along the satellite track [Benson et al., 2006].

The RPI on IMAGE is the first WM wave sounder in space. WM echoes observed by RPI on IMAGE at altitudes less than 5,000 km have led to powerful new and unique remote sensing techniques of Ne, relative ion composition (H+, He+ and O+), and FAI [Carpenter et al., 2003; Sonwalkar et al., 2004; Sonwalkar et al., 2006]. Sonwalkar et al. [2004] have shown that diffuse and discrete WM echoes can be used to find Ne, ΔNe, and scale sizes of FAI, along the field line passing through the satellite at altitudes less than 5000 km. Recent work on MR (magnetospherically reflected) whistlers observed by RPI/IMAGE by Sonwalkar et al. [2006] has shown that accurate measurements of the relative ion compositions of H+, He+ and O+ can be made along the field line passing through the satellite at altitudes less then 5000 km.

Recent work on RPI/IMAGE has led to detection of electron and ion density enhancements during intense geomagnetic storms at high altitudes [Tu et al., 2007; Osherovich et al., 2007]. Osherovich et al. [2007] have calculated Ne from plasma resonances at high altitudes near the apogee of IMAGE during both when the magnetosphere is quiet and disturbed and have compared them with those calculated from existing models. They also suggest that the plasma parameter fpe/fce can be used as magnetospheric index. Tu et al. [2007] have observed enhanced density profiles along magnetic field lines in the polar cap magnetosphere during stormy times when compared with those during quiet times. Possible reasons for enhanced density during stormy times are also discussed.

This thesis presents the occurrence pattern of WM echoes observed by RPI/IMAGE at altitudes less than 5,000 km during quiet and disturbed geomagnetic conditions. This work can further lead to the study of electron densities and ion composition variations during

quiet and disturbed periods in the magnetosphere.

1.4 Significance of the work

The work presented in this thesis complements the work done on the electron density variations at high altitudes and latitudes during geomagnetically quiet and disturbed conditions. MR-WM and SR-WM echoes observed during quiet and storm times can be used to measure the electron density and relative ion composition during both stormy and quiet periods at low altitudes (<5,000 km).

The study of the WM echoing processes helps in understanding the natural WM/VLF activity in the magnetosphere.

1.5 Problem statement and approach

This thesis is built upon the work presented by Sonwalkar et al. [2007] at the URSI conference in Canada. The two important questions this thesis deals with are: the occurrence pattern of WM echoes as a function of geophysical conditions, and the effect of geomagnetic storms on WM echoing process.

A data survey during 2004 January-December 2005 was performed to identify a variety of WM echoes observed by RPI when IMAGE is at altitudes less than 5,000 km. These echoes were categorized by their reflection processes and frequency versus time delay characteristics. The occurrence patterns of these echoes were found as a function of geophysical conditions. Quiet and disturbed periods during the period of August-December 2005 were identified and a detailed analysis of WM echoes as a function of geomagnetic activity was performed.

1.6 Contributions of this thesis work

Part of the present work is reported in Sonwalkar et al. [2007]. The contributions of this thesis are listed below:

1. A data survey during the 2004 January-December 2005 period is performed and the distribution of discrete, multipath, diffuse MR- and SR-WM echoes is found.

2. A detailed analysis of selected quiet and disturbed periods during the Aug-Dec 2005 period is performed and the occurrence pattern of WM echoes (all kinds) as a function of geomagnetic activity is determined. We believe that this work will lead to a better understanding of variations in electron density, density structures and ion composition during quiet and disturbed periods.

1.7 Organization of thesis

The organization of this thesis is as follows:

Chapter 1 gives a brief introduction to the thesis topic. It talks about the past work done related to the electron density and density irregularity measurements.

Chapter 2 presents the observations and generation mechanisms of WM waves observed by RPI/IMAGE at altitudes less than 5,000 km. It also presents occurrence patterns of WM echoes as a function of geophysical conditions.

Chapter 3 discusses the occurrence pattern of WM echoes during quiet and disturbed geomagnetic conditions in the August-December 2005 period.

Chapter 4 presents the summary, discussions, and recommendations for future work.

Chapter 2 Occurrence patterns of WM echoes observed by RPI/IMAGE

The objective of this chapter is to present 1) the observations of a variety of WM echoes observed by RPI/IMAGE during the years 2004 and 2005, and 2) occurrence patterns of WM echoes. The first section of this chapter gives an introduction to WM echoes and their generation mechanisms. The second section briefly describes the IMAGE experiment and then presents the examples of a variety of WM echoes observed by RPI/IMAGE. The third section presents the occurrence pattern of WM echoes with respect to location and geomagnetic activity as indicated by Kp.

2.1 Introduction to whistler mode (WM) echoes

Whistler mode waves propagate in the magnetosphere at a frequency (f) below either the electron plasma frequency (f_{pe}) or the electron gyrofrequency (f_{ce}), whichever is lower. WM echoes can be categorized into two types based on their reflection mechanism: 1) magnetospherically reflected (MR) whistler mode (WM) echoes [Sonwalkar et al., 2006] and 2) specularly reflected (SR) whistler mode (WM) echoes [Sonwalkar et al., 2004; Sonwalkar et al., 2007]. Furthermore, based on the characteristic spectral form, WM echoes can be classified as discrete, multipath, or diffuse echoes. MR echoes are reflected at altitudes >1,000 km where the local lower hybrid frequency (f_{lh}) is equal to the transmitted pulse frequency f. The SR echoes are reflected at the Earth ionosphere boundary (altitude ≈90 km). These processes generate discrete, multipath or diffuse types of echoes depending on whether or not large/small scale irregularities are present along the propagation path.

2.1.1 Mechanisms of WM echo generation

Figure 2.1 shows various propagation scenarios that may lead to magnetospherically reflected (MR) whistler-mode (WM) echoes observed on IMAGE. Figure 2.1a shows the generation mechanism of a discrete MR-WM echo with very little or no spreading ($\leq$ 5 ms) in time delays at each frequency. This is due to propagation of RPI signals in a relatively smooth magnetosphere in the neighborhood of the geomagnetic field line (**B**) passing through IMAGE. Figure 2.1b shows the generation mechanism of a multipath MR-WM echo with medium time delay spreading ($\approx 10 - 20$ ms) at each frequency. This is due to the propagation of RPI signals along multiple paths to IMAGE in the presence of large scale ($\approx 1 - 10$ km) irregularities above ~1000 km (approximate $f_{lh,max}$ altitude) in the magnetosphere near **B**. Figure 2.1c shows the generation mechanism of a diffuse MR-WM echo with large time delay spreading ($\approx 60 - 80$ ms) at each frequency. This is due to the scattering of RPI signals by small scale (10 m - 100 m) irregularities above ~1000 km located close to **B**.

This mechanism, involving the MR process, is limited to frequencies less than the maximum f_{lh} in the magnetosphere ≈15 kHz. The lower hybrid frequency, f_{lh}, depends on f_{pe}, f_{ce}, and m_{eff}, the effective ion mass. The latter depends on the ion composition. Using ray tracing simulations, and with certain reasonable assumptions about the relative scale heights of H+, He+, and O+ ions, it is possible to infer Ne and individual ion densities along **B** [Sonwalkar et al., 2006].

Figure 2.2 shows various propagation scenarios that may lead to a specularly reflected (SR) whistler-mode (WM) echo observed on IMAGE. Figure 2.2a shows the generation mechanism of discrete SR-WM echoes with very little or no spreading ($\leq$ 5 ms) in time delays at each frequency due to the propagation of RPI signals in a relatively smooth magnetosphere in the neighborhood of **B**. Figure 2.2b shows the generation mechanism of multipath SR-WM echoes with medium time delay spreading ($\approx 10 - 20$ ms) at each frequency, due to the propagation of RPI signals along multiple paths to IMAGE in the presence of large scale ($\approx 1 - 10$ km) irregularities in the lower part of the magnetosphere.

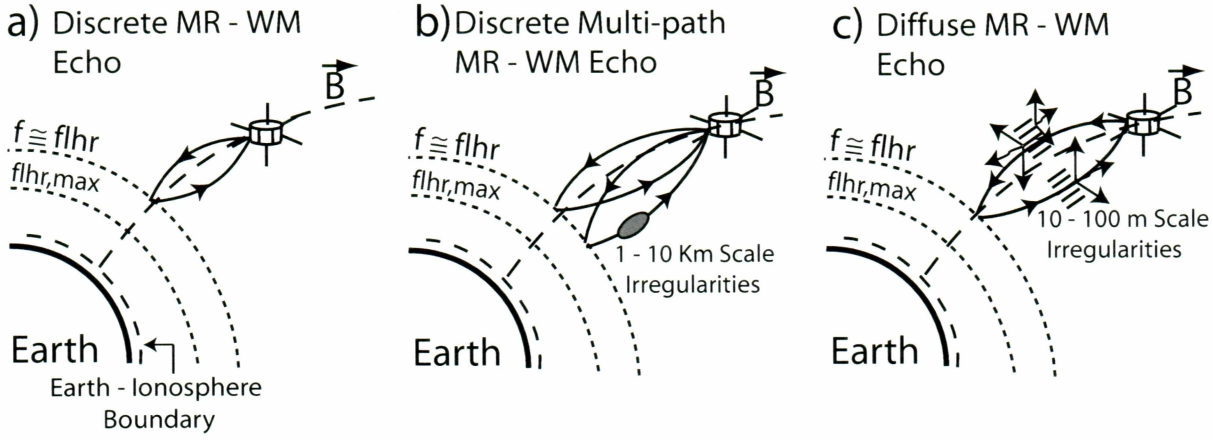

Figure 2.1. Schematic showing various propagation scenarios of MR-WM echo generation. The satellite is assumed to be located at an altitude of a few thousand km. (a) Discrete MR-WM echo. (b) Multipath MR-WM echo. (c) Diffuse MR-WM echo [Adapted from Sonwalkar et al., 2006]

Figure 2.2c shows the generation mechanism of discrete SR-WM echoes, due to the propagation of RPI signals inside field aligned ducts. Figure 2.2d shows the generation mechanism of diffuse SR-WM echoes due to the scattering of RPI signals by small scale (10-100 m) irregularities located close to **B** [*Sonwalkar et al.*, 2004].

Figure 2.3 shows the propagation scenario that may lead to back scattered (BS) whistler-mode (WM) echoes observed on IMAGE. Unlike diffuse MR and SR-WM echoes these echoes do not undergo specular or magnetospheric reflections. They are generated by the scattering of WM waves by small scale (∼10-100 m) irregularities located close to IMAGE in the direction of **B** Sonwalkar et al. [2004].

2.2 Experiment description and observations of SR- and MR-WM echoes

2.2.1 Experiment description

The IMAGE satellite was launched on 25 March 2000 into an elliptical polar orbit with apogee at $\approx 8\ R_E$, perigee at $\approx$ 1000 km altitude, and initial latitude of apogee 40N. After 5.8 years of highly successful operation, on 18 December 2005, IMAGE telemetry was not received during a routine pass, ending the mission. RPI is a multimode instrument on

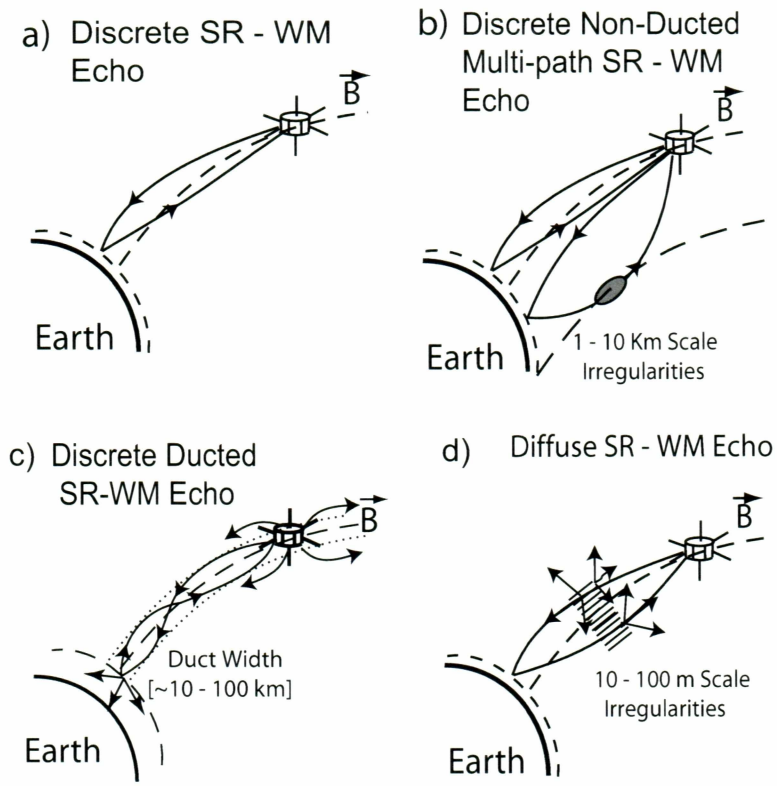

Figure 2.2. Schematic showing various propagation scenarios of SR-WM echo generation. The satellite is assumed to be located at an altitude of a few thousand km . (a) Discrete SR-WM echo. (b) Multipath SR-WM echo. (c) Ducted SR-WM echo. (d) Diffuse SR-WM echo [Adapted from Sonwalkar et al., 2004]

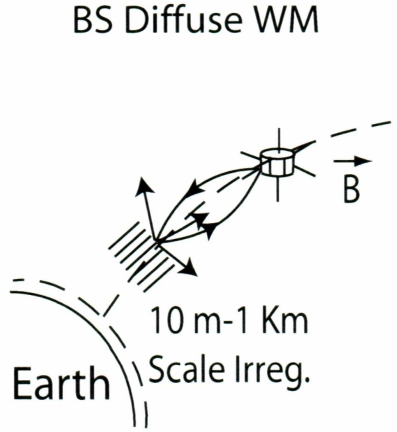

Figure 2.3. Schematic showing the propagation scenario of a BS-WM echo [Adapted from Sonwalkar et al., 2004]

IMAGE [*Reinisch et al.*, 2000] in which sounding and listening frequencies, range detection, pulse characteristics and repetition rate were adjustable parameters over a wide range of values. The instrument covered the frequency range from 3 kHz to 3 MHz with a receiver bandwidth of 300 Hz. There were three orthogonal thin wire antennas, two 500-m tip-to-tip dipoles in the spin plane (X and Y) and a 20-m tip-to-tip dipole along the spin axis (Z). The long dipoles were used for transmission, and all three antennas were used for reception [*Sonwalkar et al.*, 2004].

RPI instrument could be operated in two modes: (1) active sounding and (2) passive recording. Figure 2.4 shows the IMAGE orbit in 2005, a schematic of active sounding (left)and the passive recording experiment (right). In active sounding, RPI transmits signals and detects the echoes returning to the satellite. There were different programs in active sounding. Each program has a different frequency range, step size, and range detection. During passive recordings, the satellite only listens to the thermal noise in space.

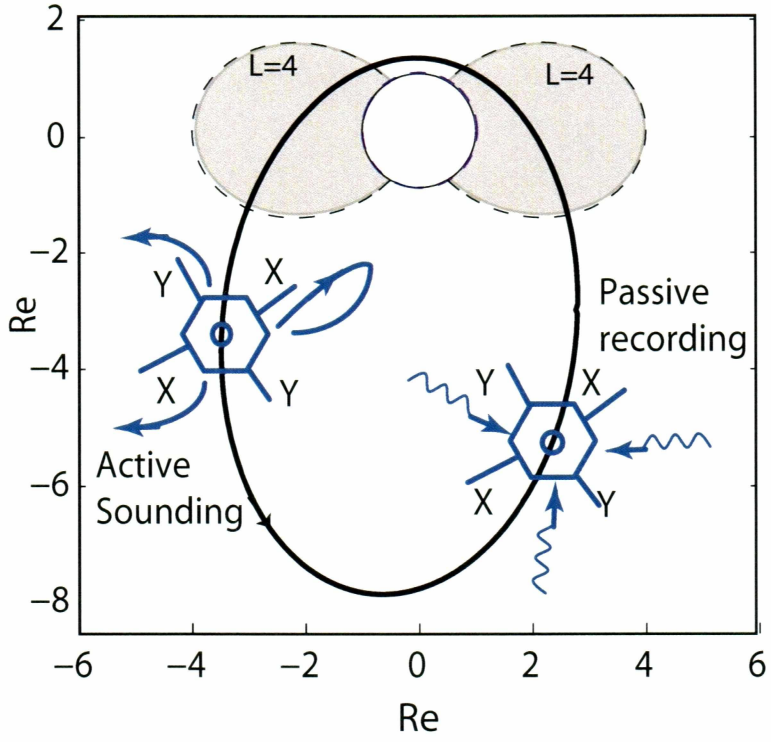

Figure 2.4. Schematic showing the RPI acitve sounding and passive recording experiments

Figure 2.6 shows examples of MR-WM and SR-WM echoes observed on the IMAGE satellite when 3.2 ms short pulses in 6-63 kHz frequency range with 0.3 kHz linear stepping (program 38) were transmitted at altitudes less than 5,000 km. Figure 2.5 shows the transmission pattern of program 38. Figure 2.6a shows the discrete trace of MR whistler-mode echoes below ≈10 kHz with time delay increasing with frequency. Discrete traces above ≈10 kHz with time delay decreasing with frequency are specularly reflected (SR) whistler mode echoes. Horizontal traces below about 40 ms time delay are proton cyclotron (PC) echoes [Carpenter et al., 2007] and the vertical traces above 10 kHz covering the entire time delay axis range are ground transmitter signals clearly visible at ∼25 kHz. The arrow on the frequency axis indicate the lower cutoff frequency of MR-WM echoes, identified as the local lower hybrid frequency (f_{lh}) [Sonwalkar et al., 2006]. Figure 2.6b shows the discrete trace of SR-WM echoes above ≈9 kHz with time delay decreasing with frequency.

The passive measurement programs are interspersed with active sounding. During typical RPI operations, a sounding program lasting from tens to hundreds of seconds is repeated at intervals of 2 to 10 min within a schedule containing other programs and passive recordings [Reinisch et al., 2000]. Passive measurements (Figure 2.7) provide important information on local plasma density, plasmapause location, natural plasma wave activity, and the reception of the ground transmitter signals. Knowledge of background natural plasma wave activity is important because often times echoes from active sounding are not observed because they are masked by natural background.

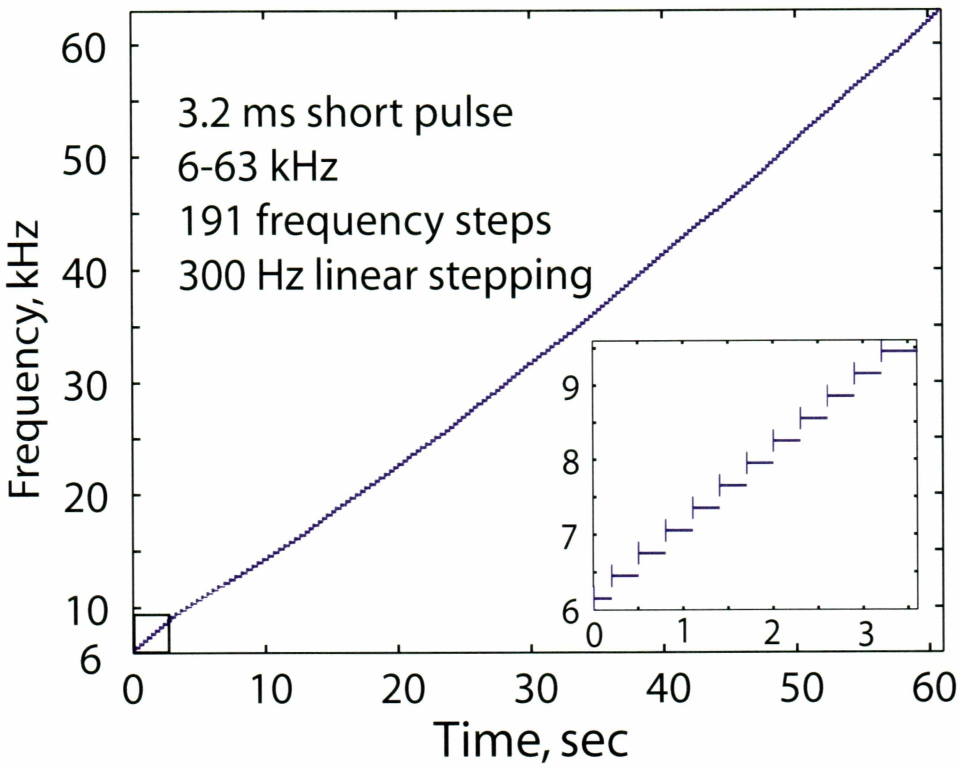

Figure 2.5. The frequency step and time step of transmitted signal in the active sounding program 38. The inset shows the details of the program. The vertical line at the beginning of each horizontal line represents 3.2 ms duration transmitted pulse at that frequency. The length of the horizontal line represents the waiting period during which RPI listens to the echoes

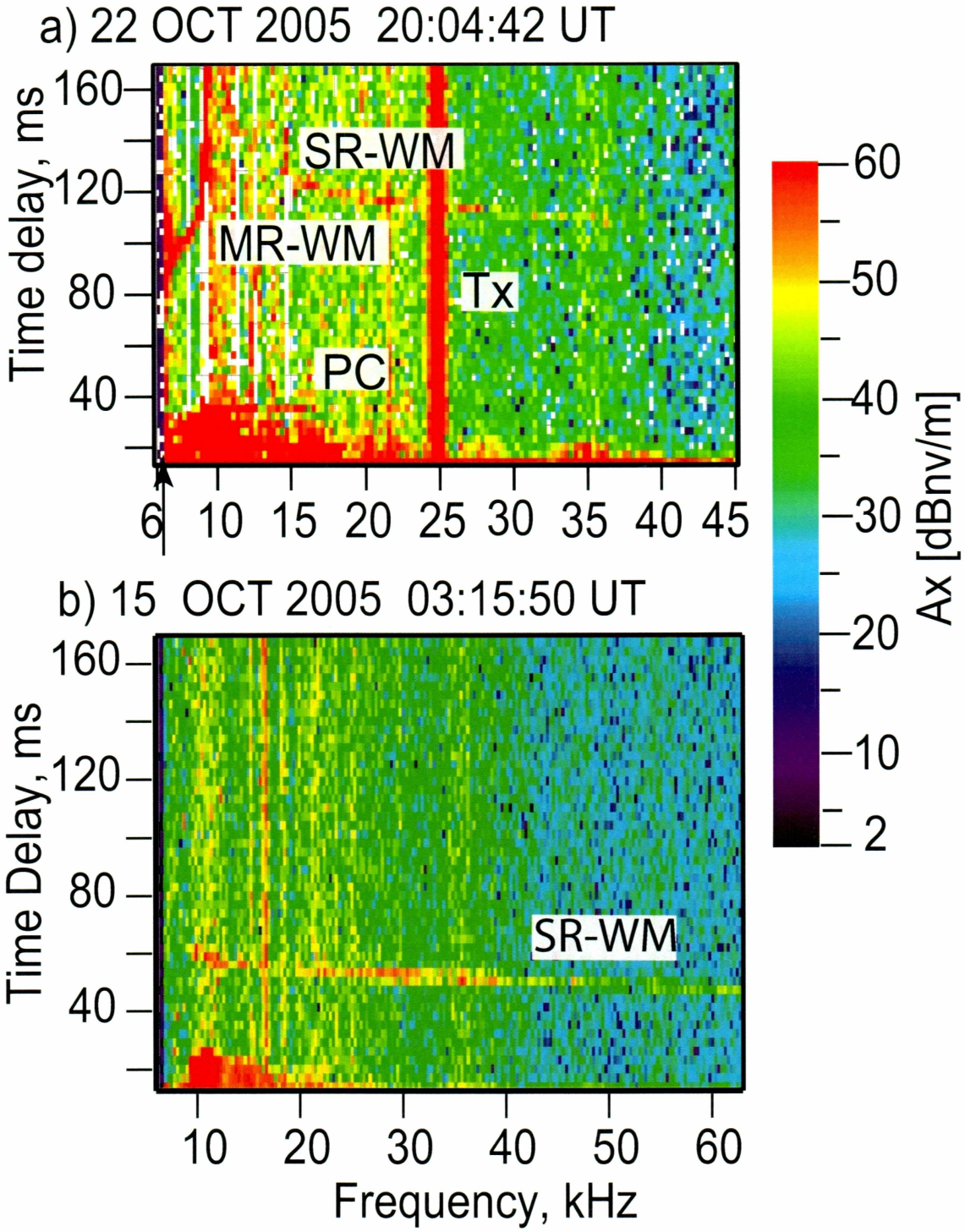

Figure 2.6. Examples of magnetospherically reflected (MR) and specularly reflected whistler mode echoes received during soundings by RPI in October, 2005. (a-b) Plasmagrams displaying time delay versus frequency for whistler-mode echoes received on 15 October and 22 October 2005, respectively

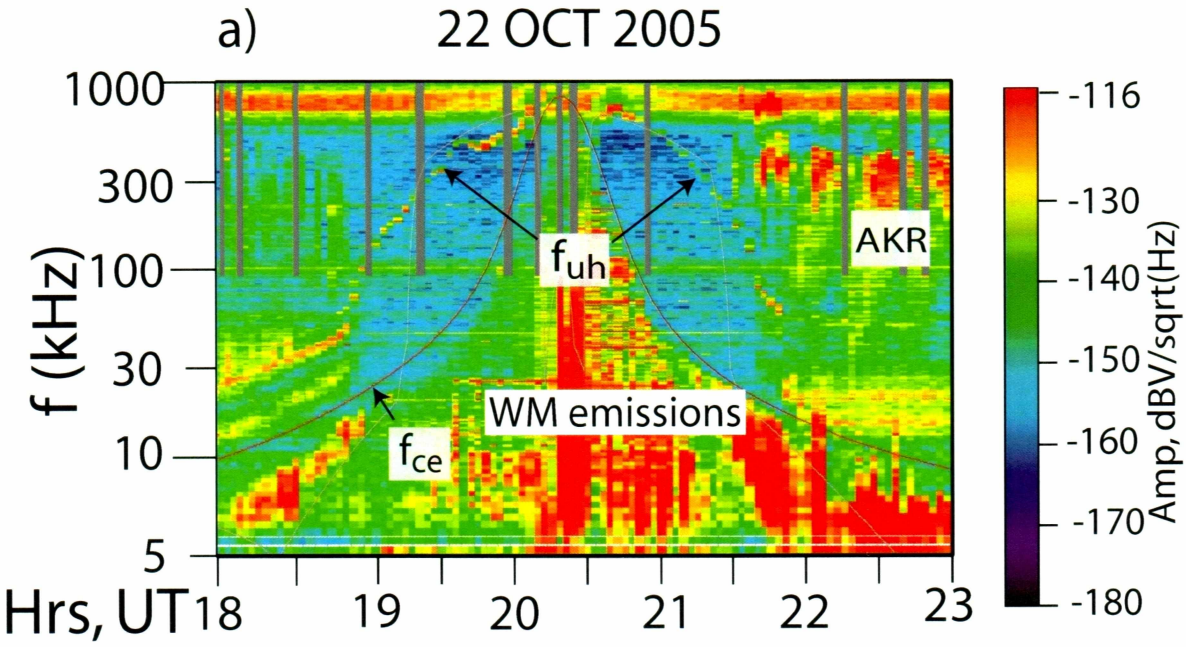

Figure 2.7. An example of RPI passive sounding recordings. The dynamic spectrum shown here is constructed by synthesis of passive measurements for the entire orbit. The upper hybrid emission provides a measure of f_{pe}. The sudden drop in the upper hybrid emission frequency (f_{uh}) can be used to determine the plasmapause location. The red curve gives the values of gyro frequency (f_{ce}) at that time

2.2.2 Observations

During the years 2004 and 2005, when IMAGE was at low altitudes (<5,000 km), program 38 was transmitted and a variety of WM echoes were observed by RPI/IMAGE. This section illustrates various features of WM echoes and their occurrence patterns.

2.2.2.1 Examples of variety of MR-WM echoes observed by RPI/IMAGE

Figure 2.8 shows examples of MR-WM echoes and illustrates various features of MR-WM echoes. Figure 2.8a shows an MR-WM echo characterized by a lower cutoff frequency, f_l, at 6.3 kHz, a higher cutoff frequency, f_u, at 10.8 kHz, and a minimum time delay at 8.1 kHz. The satellite was at 3420 km altitude, 14.2°N magnetic latitude and 10.0 MLT. These echoes were always accompanied by PC echoes [Carpenter et al., 2007], separated by the proton gyro period tp which provides an estimate of the local gyro frequency, f_{ce}.

Figure 2.8b shows an example of a discrete MR-WM echo appearing without a minimum in time delay. This echo is characterized by a lower cutoff frequency, f_l, at 6.9 kHz, a higher cutoff frequency, f_u, at 10.2 kHz. This echo is observed when the satellite is located at 2948 km altitude, 31.6°N magnetic latitude, and 10.8 MLT. The horizontal traces below 45 ms time delay are PC echoes.

Echoes such as these in Figure 2.8a-b, with well defined time delay as a function of frequency and relatively small spreading in time delays at each frequency, are called discrete MR-WM echoes. These result from magnetospheric reflections of RPI signals as illustrated by figure 2.1a

Figure 2.8c shows an example of a discrete multipath MR-WM echo with about a 20 ms spread in time delay at each frequency. This echo is characterized by a lower cutoff frequency, f_l, at 7.8 kHz, and a higher cutoff frequency, f_u, at 10.5 kHz. This echo is observed when the satellite is located at 2654 km altitude, 39.24°N magnetic latitude, and 12.3 MLT. The horizontal traces below 40 ms time delay are PC echoes. It is interpreted that these echoes have resulted from RPI signals propagating downwards in a magnetosphere containing 1-10 km scale irregularities, undergoing magnetospheric reflection, and reaching

back to the satellite via multiple paths, as illustrated by figure 2.1b.

Figure 2.8d shows an example of a diffuse MR-WM echo with more than 80 ms spread in time delay at each frequency, generally seen at low altitudes (< 3000 km). This echo is characterized by a lower cutoff frequency, f_l, at 8.7 kHz, a higher cutoff frequency, f_u, at 11.1 kHz. This echo is observed when the satellite is located at 2490 km altitude, 38.52°N magnetic latitude, and 11.9 MLT. The horizontal traces below 40 ms time delay are PC echoes. Figure 2.8e shows an example of a diffuse MR-WM echo without a well-defined outline. This echo is characterized by a lower cutoff frequency, f_l, at 8.4 kHz, and a higher cutoff frequency, f_u, at 11.4 kHz. This echo is observed when the satellite is located at 2576 km altitude, 40.7°N magnetic latitude, and 2.65 MLT. Echoes such as these have resulted from RPI signals propagating downwards in a magnetosphere containing 10-100 m scale size irregularities which are present in the magnetosphere close to B. RPI signals are forward scattered, then undergo magnetospheric reflection, again get forward scattered, and come back to the satellite via multiple paths, as illustrated by Figure 2.1c. Diffuse MR-WM echoes are often accompanied by discrete SR-WM echoes (appearing in the 13-30 kHz frequency range in Figure 2.8d and 25-30 kHz frequency range in figure 2.8e, but extending to 63 kHz), which result from the reflection of RPI signals at the Earth-ionosphere boundary [Sonwalkar et al., 2004]. Figure 2.8f shows plot of the low-altitude portion of the IMAGE satellite orbit on 16 Nov 2005. The vertical bands at fixed frequencies seen on Figure 2.8b-2.8f are ground VLF transmitter signals [Sonwalkar et al., 2006].

It can be observed that the arrow marks on the frequency axis which indicate the local f_{lh} move towards higher frequencies as we go from figure 2.8a-e. This indicates that, as we go to lower altitudes, f_{lh} increases.

2.2.2.2 Examples of variety of SR-WM echoes observed by RPI/IMAGE

Figure 2.9a shows a plasmagram displaying SR-WM echoes above ≈10 kHz. Figure 2.9b shows SR-WM echo ≈ above 9.6 kHz accompanying an MR-WM echo below ≈9.6 kHz. In cases such as these the lower cutoff of SR-WM echo provides a measure/limitation on the

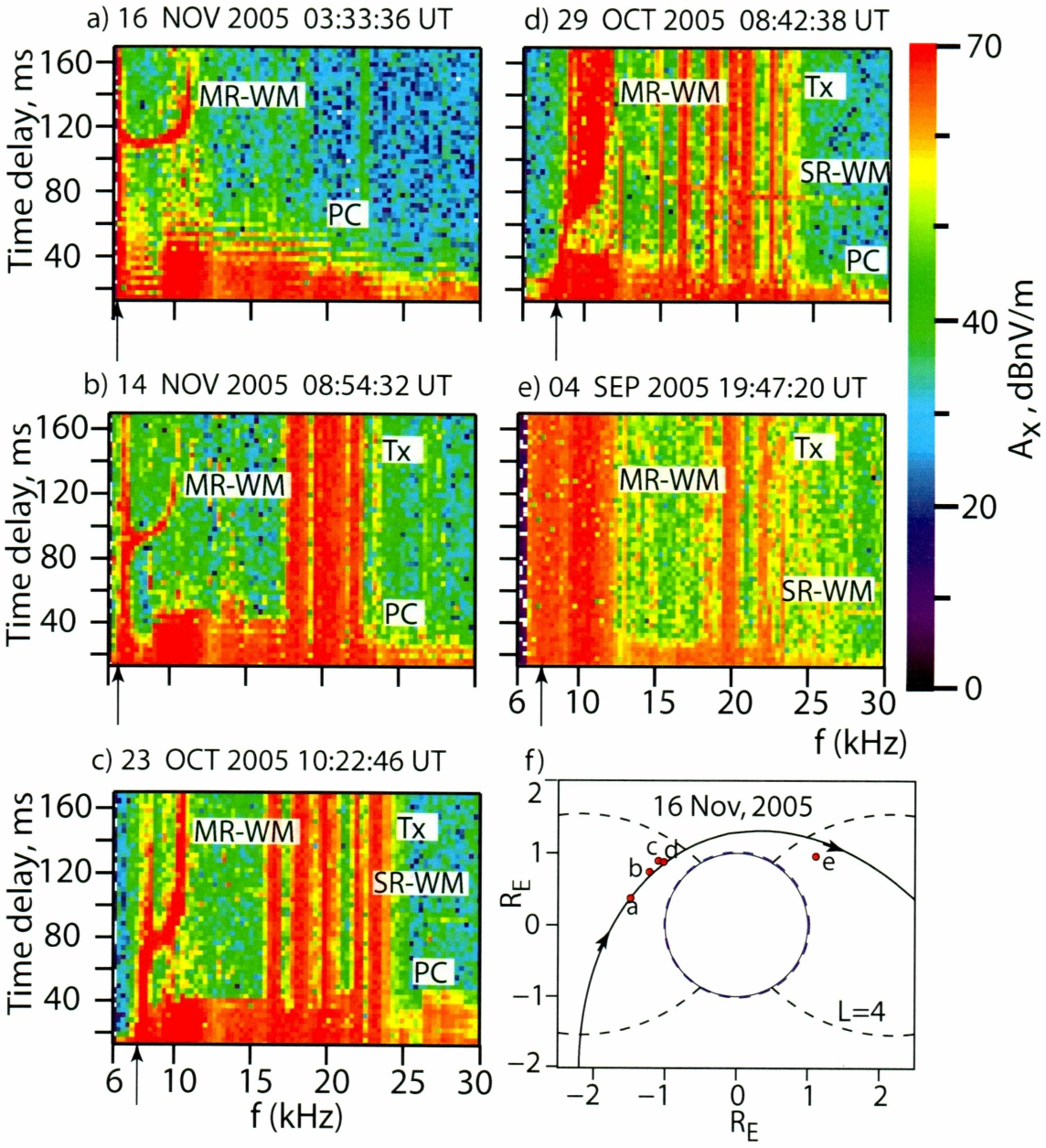

Figure 2.8. RPI plasmagrams illustrating various types and features of MR-WM echoes seen on the IMAGE satellite. (a) A discrete MR-WM echo showing a minimum in time delay, (b) a discrete MR-WM echo showing no minimum in time delay, (c) discrete MR-WM echoes occurring with multiple time delays at each frequency, (d) diffuse MR-WM echoes with characteristic MR-WM echoes shape (as seen in a, b, and c) and with large spread in time delay (>80 ms) at each frequency, (e) diffuse MR-WM echoes with poorly defined outline, and with large time delays (>160 ms), covering the entire time delay axis, at each frequency, (f) plot of the low-altitude portion of the IMAGE polar orbit for the case of Figure 8a. The approximate locations of IMAGE for the five cases are indicated by red dots. Dipole field lines at L = 4 are shown as a reference Adapted from Sonwalkar et al., 2006

$f_{lh,max}$ along the L=shell passing through IMAGE. Echoes such as these (Figure 2.9a and 2.9b) with well defined time delay as a function of frequency and with relatively small spreading in time delays say less than 6 ms at each frequency are called discrete SR-WM echoes. These echoes are generated by RPI signals specularly reflecting at the Earth ionosphere boundary ≈90 km as illustrated by figure 2.2a. Figure 2.9c shows an example of SR-WM echo above ≈9.9 kHz frequency. Echoes such as these whose time delay at each frequency is ≈20 ms are called multipath SR-WM echoes. It is interpreted that these echoes are observed when RPI signals undergoing specular reflection at the Earths ionosphere boundary ≈90 km and encountering large scale irregularities present in the magnetosphere close to B in their propagation path and coming back to satellite via multiple paths as illustrated in figure 2.2b. Also in this example, the frequencies 30-50 kHz display time delays going up to 80 ms, this could be evidence of the forward scattering of signals. This mechanism is explained using figure 2.9d. Figure 2.9d shows an example of SR-WM echo at frequencies greater than ≈10 kHz. Echoes such as these, whose time delay at each frequency ranges from 40-80 ms, are called diffuse SR-WM echoes. Echoes such as these are generated when RPI signals encounter small scale irregularities (10 m-1 km) in their propagation path, get forward scattered, reflect at the earth ionosphere boundary, and come back to satellite via multiple paths as illustrated in figure 2.2d.

2.2.2.3 Examples of BS-WM echoes observed by RPI/IMAGE

Figure 2.10 shows an example of a WM echo, in the frequency range of 10-20 kHz, which is generated by back scattering of WM signals due to the presence of small scale irregularities close to the location of IMAGE and B. These back scattered RPI signals come back to the satellite via multipaths as illustrated by Figure 2.3. In this figure we also see the evidence of SR-WM echoes whose time delays are higher than the BS-WM echo. In the case of BS-WM echoes, the RPI signals undergo diffuse reflections close to B. Therefore, we expect the time delays of BS-WM to be lower than SR-WM.

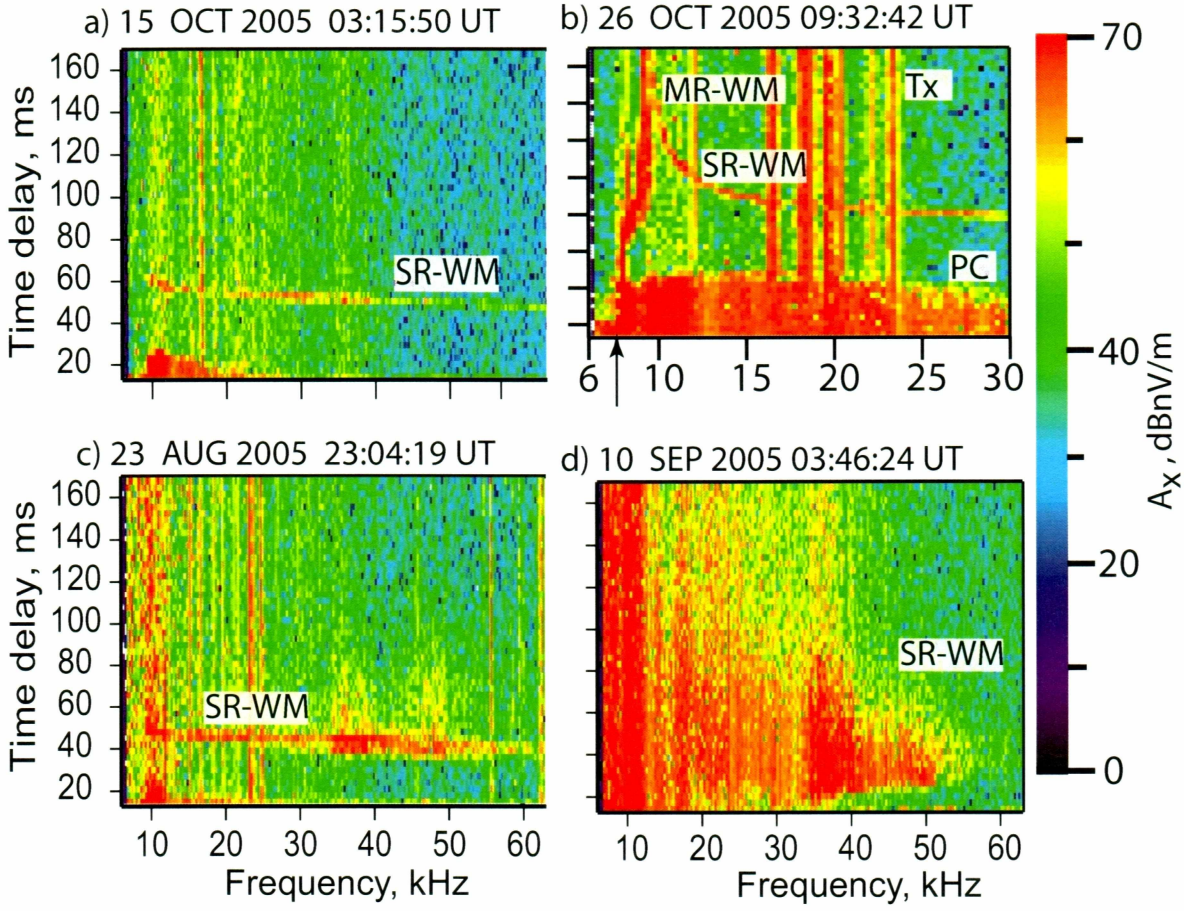

Figure 2.9. Examples of variety of SR-WM echoes observed on the IMAGE satellite. (a) Discrete SR-WM echo. (b) Discrete SR-WM echo accompanying MR-WM echo. (c) Multi-path SR-WM echo. (d) Diffuse SR-WM echo

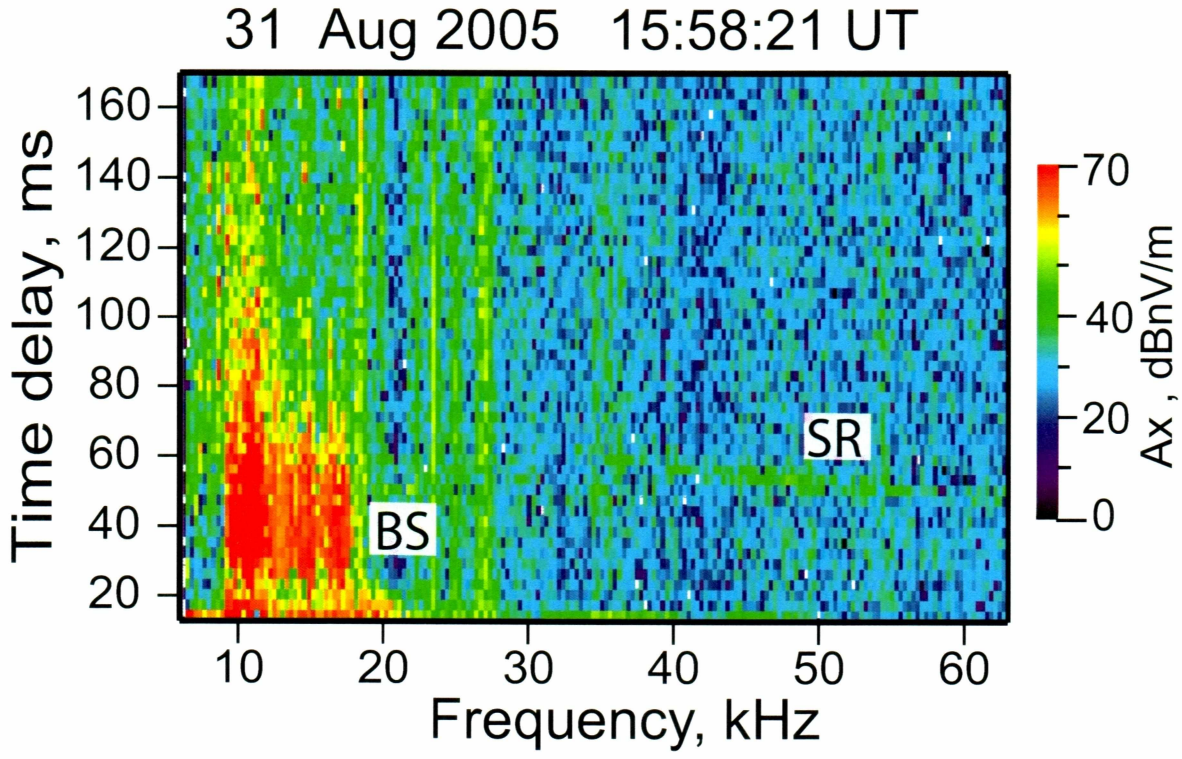

Figure 2.10. Example of back scattered diffuse WM echo observed on the IMAGE satellite

2.2.2.4 Examples of diffuse SR-WM echoes accompanying MR-WM echoes

Figure 2.11 shows plasmagrams displaying varieties of MR-WM echoes accompanied by SR-WM echoes. Figure 2.11a shows an example of a discrete MR-WM echo accompanied by a diffuse SR-WM echo. It is suggested that echoes such as these are observed when small scale irregularities are present at altitudes below 1000 km ($f_{lh,max} altitude$). A combination of mechanisms shown in figures 2.1a and 2.2d can be used to illustrate this echo. Figure 2.11b shows an example of a diffuse MR-WM echo accompanied by a diffuse SR-WM echo. It is suggested that echoes such as these are observed when small scale irregularities are present at altitudes above 1000 km ($f_{lh,max} altitude$). A combination of mechanisms shown in figure 2.1c and 2.2d can be used to illustrate this echo.

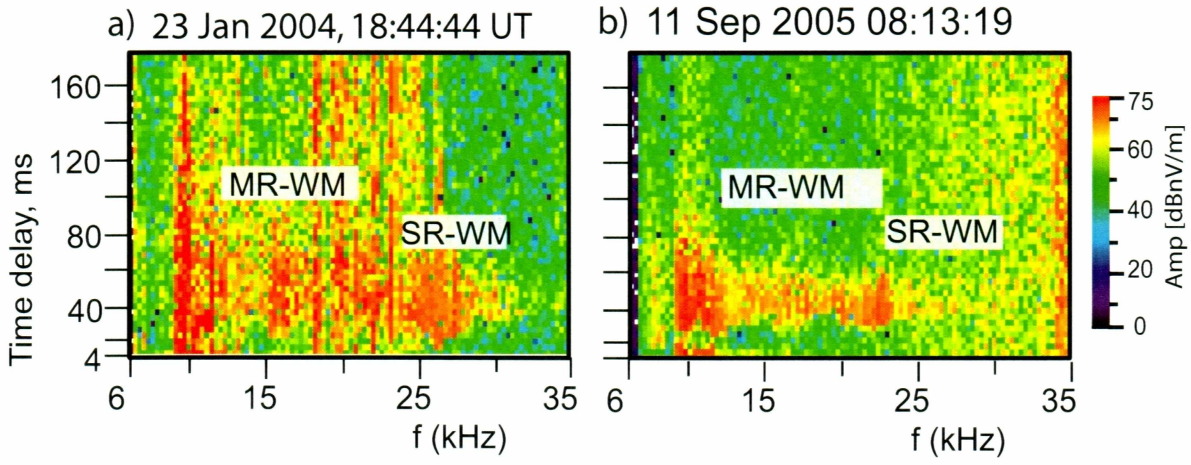

Figure 2.11. Examples illustrating varieties of MR-WM accompanied by SR-WM echoes. (a)Discrete MR-WM echo accompanied by diffuse SR-WM echo. (b)Diffuse MR-WM echo accompanied by diffuse SR-WM echo

2.3 Occurrence pattern of MR and SR- WM echoes

This subsection presents the occurrence pattern of MR- and SR-WM echoes observed on IMAGE in the period of January-August 2004 and August-December 2005 when program

38 was transmitted. The first part of this section provides the occurrence pattern of discrete MR- and SR-WM echoes, the second part provides the occurrence pattern of multipath MR- and SR-WM echoes and the last part provides the occurrence pattern of diffuse MR- and SR-WM echoes.

2.3.1 Occurrence pattern of discrete MR and SR-WM echoes

Figure 2.12 shows the occurrence pattern of discrete MR- and SR-WM echoes. Though discrete MR-WM echoes (2.12a) are found at all latitudes, they are observed more commonly inside the plasmasphere. Discrete SR-WM echoes (2.12b) are more common at lower latitudes including the plasmasphere and plasmapause region and not so common in the polar region.

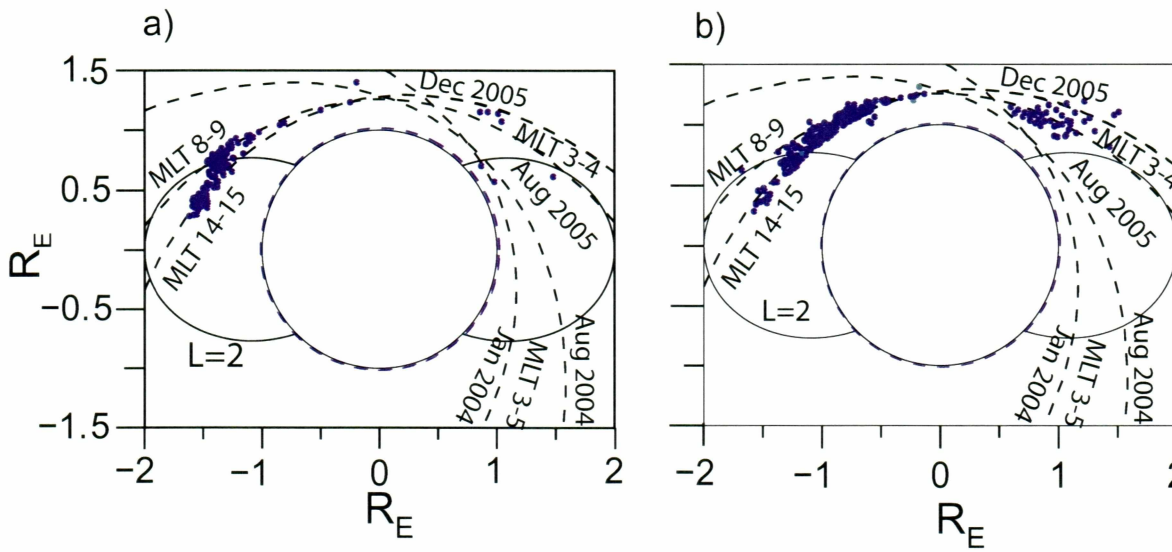

Figure 2.12. Occurrence pattern of (a) discrete MR-WM and (b) discrete SR- WM echoes

2.3.2 Occurrence pattern of multipath MR and SR-WM echoes

Figure 2.13 shows the occurrence pattern of multipath MR- and SR-WM echoes. Multipath MR-WM echoes (2.13a) are more common at low latitudes, inside the plasmasphere.

Multipath SR-WM echoes (2.13b) are found at all latitudes but are not so common in the polar region.

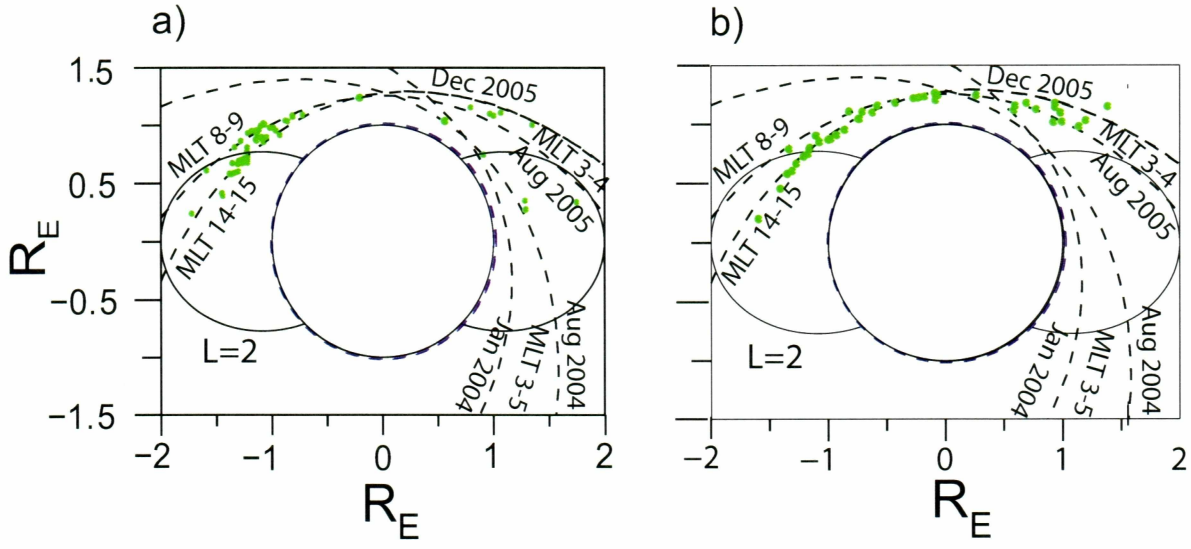

Figure 2.13. Occurrence pattern of (a) multipath MR-WM and (b) multipath SR-WM echoes

2.3.3 Occurrence pattern of diffuse MR- and SR-WM echoes

Figure 2.14 shows the occurrence pattern of diffuse MR- and SR-WM echoes. Diffuse MR-WM echoes are found at all latitudes 2.14(a). In this figure, we get the impression that there are fewer diffuse MR-WM echoes at high latitudes. This is because 1) we have fewer transmissions at higher latitudes, and 2) the echo is masked by natural noise such as auroral hiss at higher latitudes. The diffuse SR-WM echoes are found predominantly at high latitude regions including outside of the plasmapause region, subauroral, auroral, and polar regions at altitudes less than 2,500 km (2.14b).

Fewer WM echoes (all kinds) were observed during 2004. This is because there were fewer transmissions (100) of program 38 in 2004, in contrast 23 soundings on every orbit during Aug-Dec 2005. WM echoes were observed at all MLT. On one side of the orbit, MLT was 3-5 and, on the other side, MLT was 8-9 in Aug 2005 and 14-15 in Dec 2005; over the

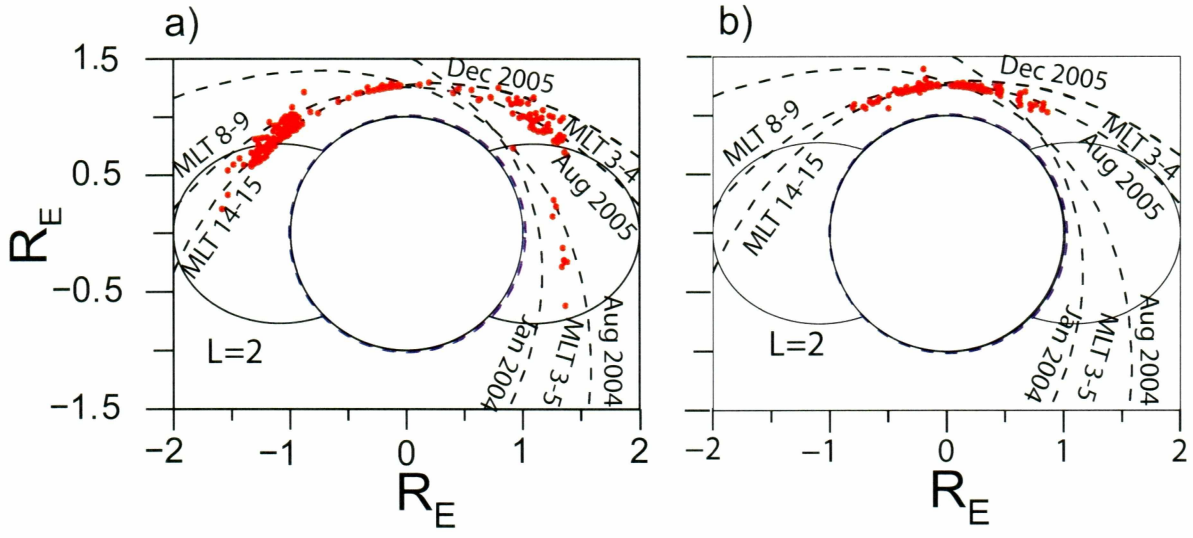

Figure 2.14. Occurrence pattern of diffuse MR- and diffuse SR- WM echoes

pole MLT changes from dawn to dusk.

2.3.4 Occurrence pattern of WM echoes with respect to Kp

This subsection presents the occurrence pattern of WM echoes, MR- and SR-WM echoes, discrete, multipath, and diffuse MR- and SR-WM echoes as a function geomagnetic activity when program 38 was transmitted at altitudes less than 5,000 km. The data set used was from the periods January-August 2004, January 2005, and August-December 2005.

Figure 2.15 shows the number of transmissions made (N_{Tx}) at and the number of plasmagrams displaying WM echoes (N_{WM}) as a function of $K_{p,max}$ in the previous 24 hours. Figure 2.16 shows the occurrence ratio of the number of transmissions made to the number of plasmagrams displaying WM echoes. It can be observed that more than 300 transmissions were made at Kp<5 but, at higher values of Kp, the transmissions made were less than 100. Therefore, the conclusions made from this and further subsections are based on the WM echoes observed at moderate values of Kp.

From the Figures 2.15 and 2.16, plasmagrams displaying WM echoes exist ≈28% of the time.

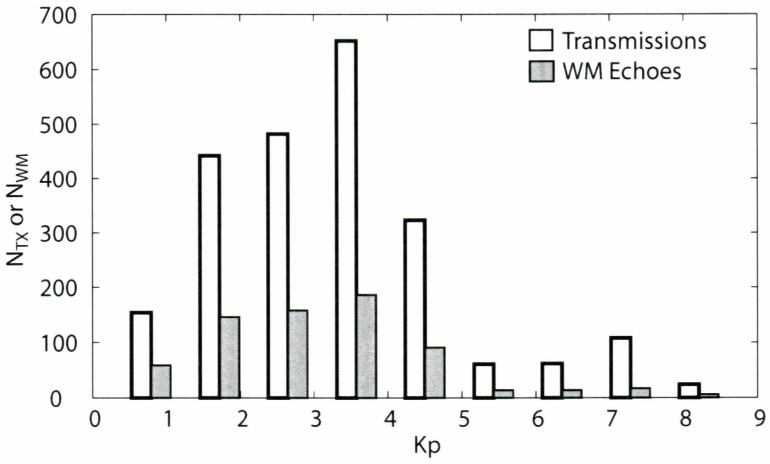

Figure 2.15. Histogram showing the numbers of program 38 transmissions and WM echoes received on IMAGE as a function of $K_{p,max}$ in the previous 24 hours

Figure 2.17 shows the number of transmissions made and the number of plasmagrams displaying WM echoes as a function of $K_{p,max}$ in the previous 12 hours. This figure has the same pattern as that of Figure 2.15. Figure 2.18 shows the occurrence ratio of the number

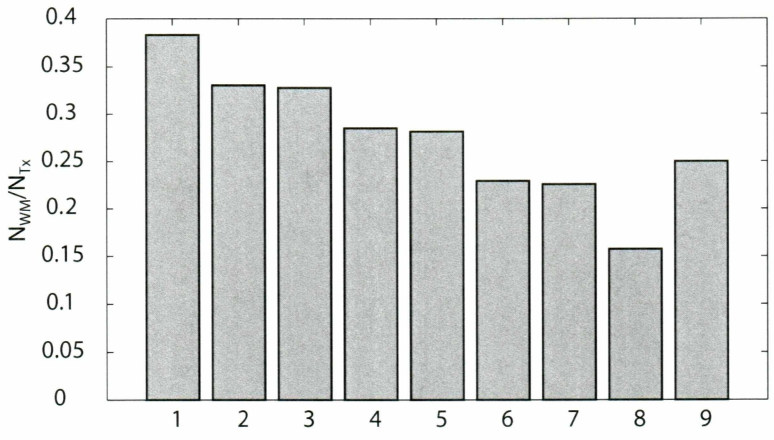

Figure 2.16. Occurrence rate in percentage of the WM echoes considering Kp from previous 24 hrs

of transmissions made to the number of plasmagrams displaying WM echoes.

From the figures 2.17 and 2.18, plasmagrams displaying WM echoes exist ≈28% of the time.

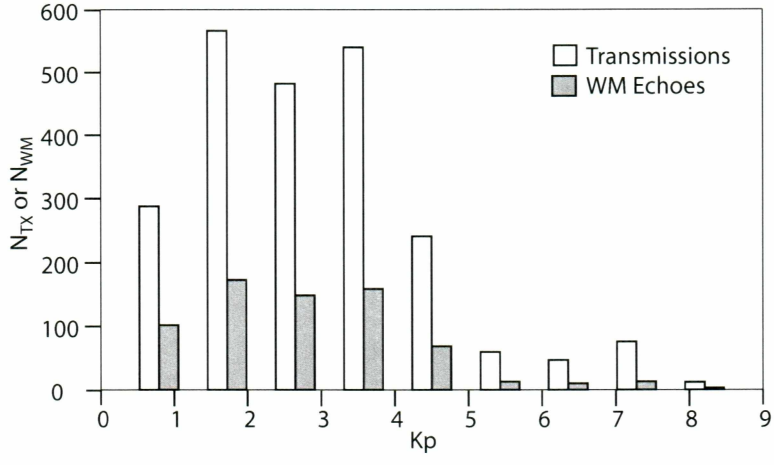

Figure 2.17. Histogram showing the numbers of program 38 transmissions and WM echoes received on IMAGE as a function of $K_{p,max}$ in the previous 12 hours

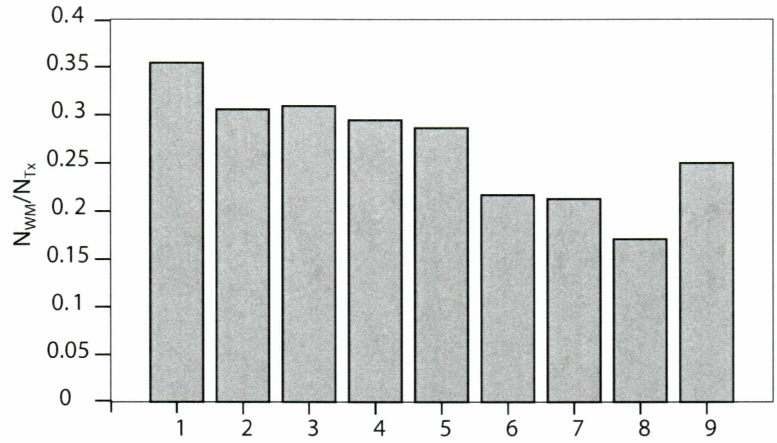

Figure 2.18. Occurrence rate in percentage of the WM echoes considering Kp from previous 12 hrs

2.3.4.1 Occurrence pattern of MR- and SR-WM echoes with respect to Kp

Figure 2.19 shows the number of transmissions made and the number of MR (N_{MR}) and SR-WM (N_{SR}) echoes observed by RPI/IMAGE as a function of $K_{p,max}$ in the previous 24 hours. Figure 2.20 shows the occurrence ratio of the number of transmissions made to the number of MR and SR-WM echoes observed.

From the figures 2.19 and 2.20, MR-WM echoes are observed ≈18% of the time and SR-WM echoes are observed ≈20% of the time.

Figure 2.21 shows the number of transmissions made and the number of MR and SR-WM echoes observed by RPI/IMAGE as a function of $K_{p,max}$ in the previous 12 hours. This figure has the same pattern as that of figure 2.19. Figure 2.22 shows the occurrence ratio of the number of transmissions made to the number of MR and SR-WM echoes observed.

From the figures 2.21 and 2.22, MR-WM echoes are observed ≈18% of the time and SR-WM echoes are observed ≈20% of the time.

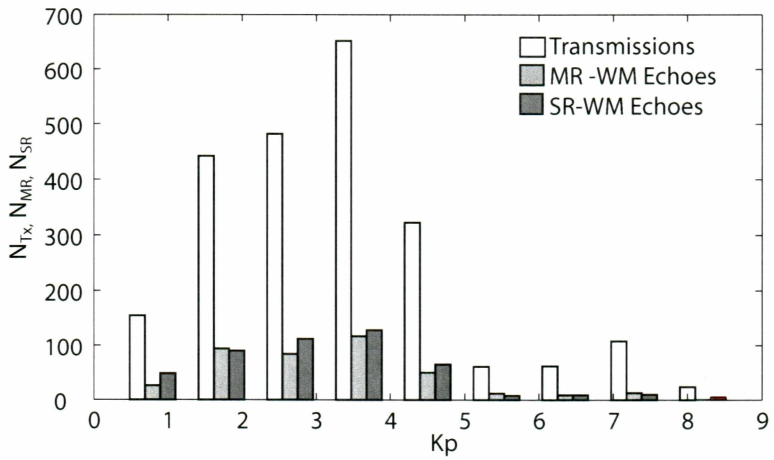

Figure 2.19. Histogram showing the numbers of program 38 transmissions and MR- and SR-WM echoes received on IMAGE as a function of $K_{p,max}$ in the previous 24 hours

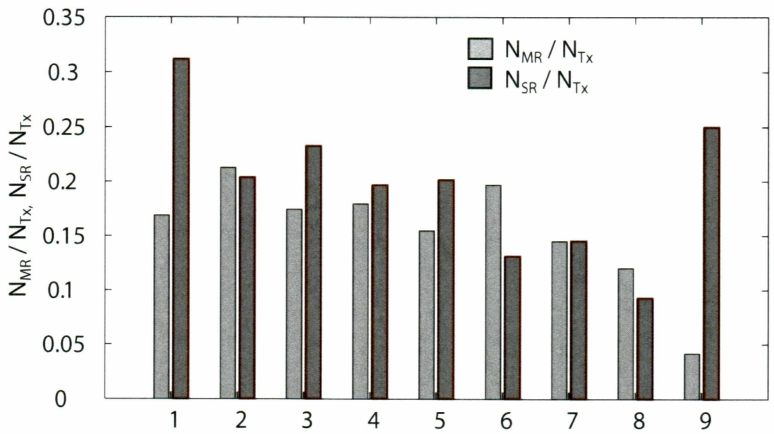

Figure 2.20. Occurrence rate in percentage of the MR- and SR-WM echoes considering Kp from previous 24 hrs

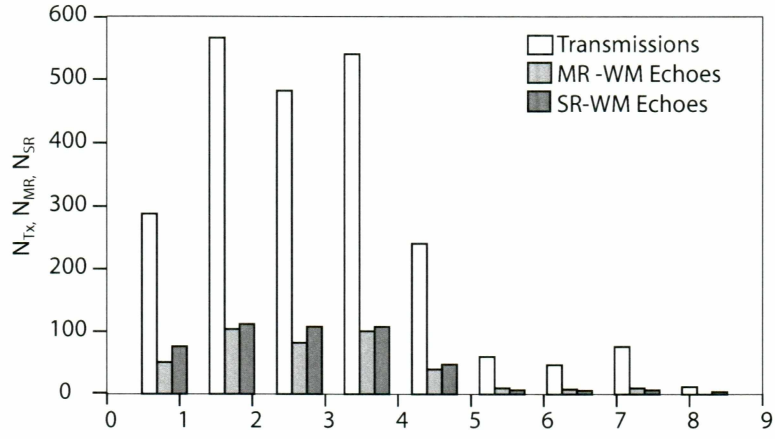

Figure 2.21. Histogram showing the numbers of program 38 transmissions and MR- and SR-WM echoes received on IMAGE as a function of $K_{p,max}$ in the previous 12 hours

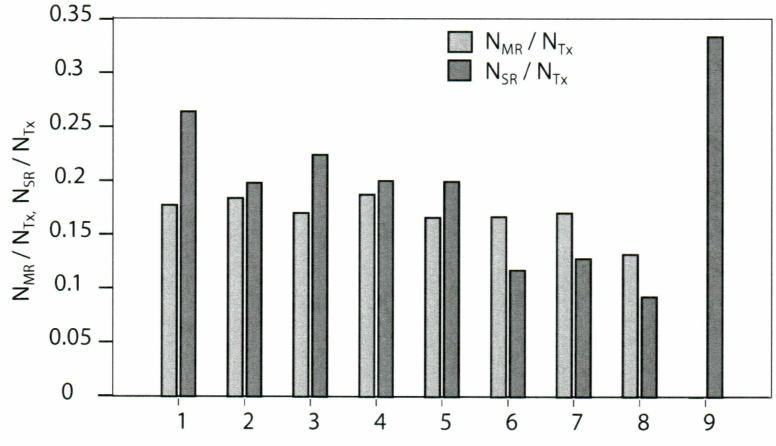

Figure 2.22. Occurrence rate in percentage of the MR- and SR-WM echoes considering Kp from previous 12 hrs

2.3.4.2 Occurrence pattern of discrete, multipath, and diffuse MR-WM echoes with respect to Kp

Figure 2.23 shows the number of program 38 transmissions made at altitudes less than 5,000 km and the number of discrete ($N_{Dis,MR}$), multipath ($N_{Mul,MR}$), and diffuse MR-WM ($N_{Diff,MR}$) echoes observed by RPI/IMAGE as a function of $K_{p,max}$ in the previous 24 hours. Figure 2.24 shows the occurrence ratio of the number of transmissions made to the number of discrete, multipath, and diffuse MR and SR-WM echoes observed.

From the figures 2.23 and 2.24, discrete MR-WM echoes are observed $\approx$5%, multipath MR-WM echoes are observed $\lesssim$1%, and diffuse MR-WM echoes are observed $\approx$11% of the time.

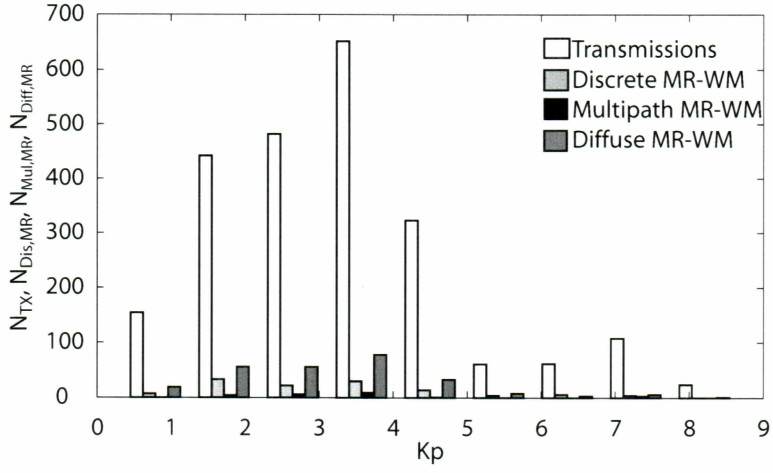

Figure 2.23. Histogram showing the numbers of program 38 transmissions and discrete, multipath and diffuse MR-WM echoes received on IMAGE as a function of $K_{p,max}$ in the previous 24 hours

Figure 2.25 shows the number of transmissions made and the number of discrete, multipath, and diffuse MR-WM echoes observed by RPI/IMAGE as a function of $K_{p,max}$ in the previous 12 hours. This figure has the same pattern as Figure 2.23. Figure 2.26 shows the occurrence ratio of the number of transmissions made to the number of discrete, multipath, and diffuse MR and SR-WM echoes observed.

From the figures 2.25 and 2.26, discrete MR-WM echoes are observed $\approx$5%, multipath

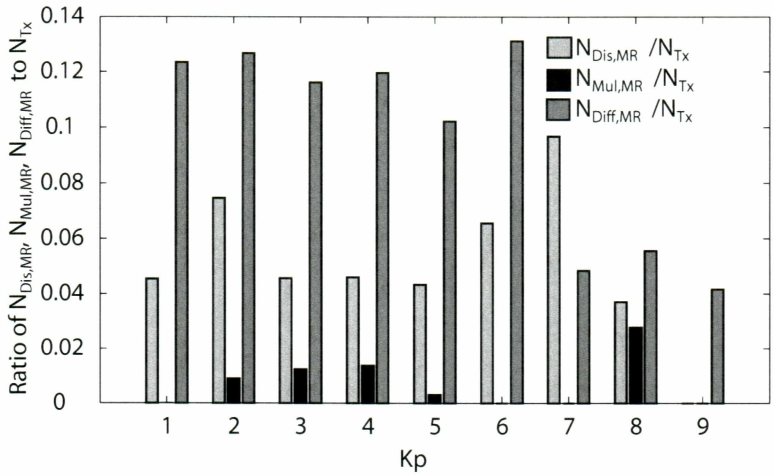

Figure 2.24. Occurrence rate in percentage of the discrete, multipath and diffuse MR-WM echoes considering Kp from previous 24 hrs

MR-WM echoes are observed $\lesssim$1%, and diffuse MR-WM echoes are observed $\approx$12% of the time.

Figure 2.27 shows the number of transmissions made and the number of discrete ($N_{Dis,SR}$), multipath ($N_{Mul,SR}$), and diffuse SR-WM ($N_{Diff,SR}$) echoes observed by RPI/IMAGE as a function of $K_{p,max}$ in the previous 24 hours. Figure 2.28 shows the occurrence ratio of the number of MR and SR-WM echoes observed to the number of transmissions made.

From the Figures 2.27 and 2.28, discrete SR-WM echoes are observed $\approx$13%, multipath SR-WM echoes are observed $\approx$2%, and diffuse SR-WM echoes are observed $\approx$6% of the time.

2.3.4.3 Occurrence pattern of discrete, multipath, and diffuse SR-WM echoes with respect to Kp

Figure 2.29 shows the number of transmissions made and the number of discrete, multipath, and diffuse SR-WM echoes observed by RPI/IMAGE as a function of $K_{p,max}$ in the previous 12 hours. Figure 2.30 shows the occurrence ratio of the number of MR and SR-WM echoes observed to the number of transmissions made.

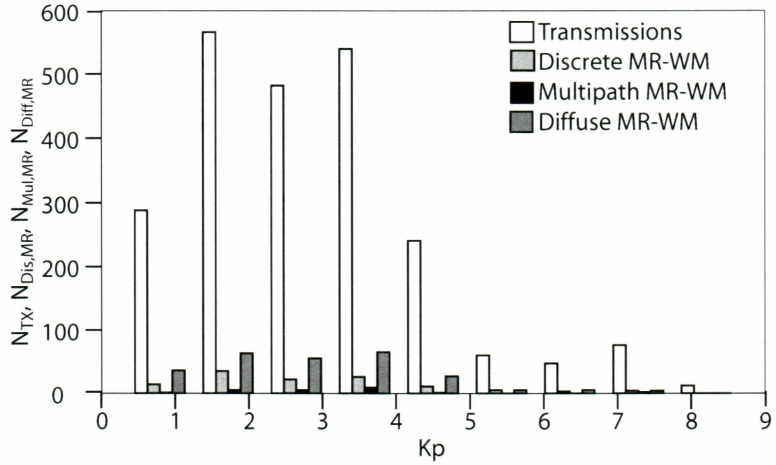

Figure 2.25. Histogram showing the numbers of program 38 transmissions and discrete, multipath and diffuse MR-WM echoes received on IMAGE as a function of $K_{p,max}$ in the previous 12 hours

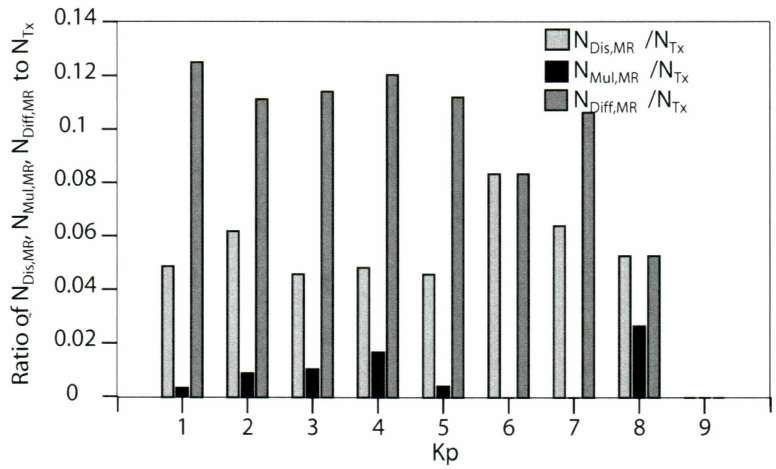

Figure 2.26. Occurrence rate in percentage of the discrete, multipath and diffuse MR-WM echoes considering Kp from previous 12 hrs

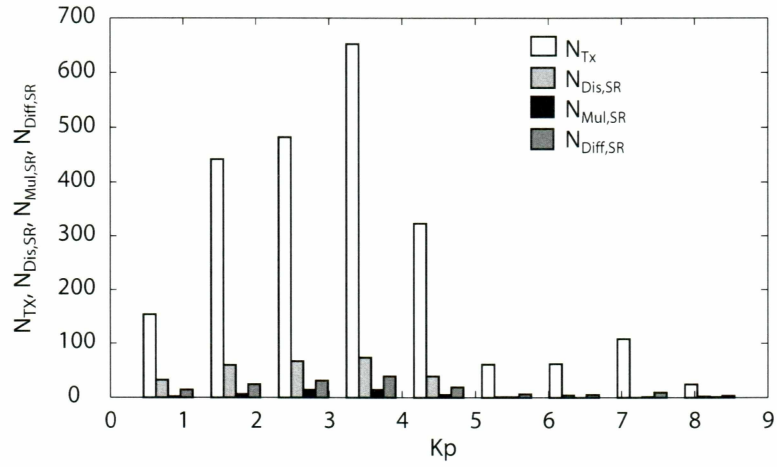

Figure 2.27. Histogram showing the numbers of program 38 transmissions and discrete, multipath and diffuse SR-WM echoes received on IMAGE as a function of $K_{p,max}$ in the previous 24 hours

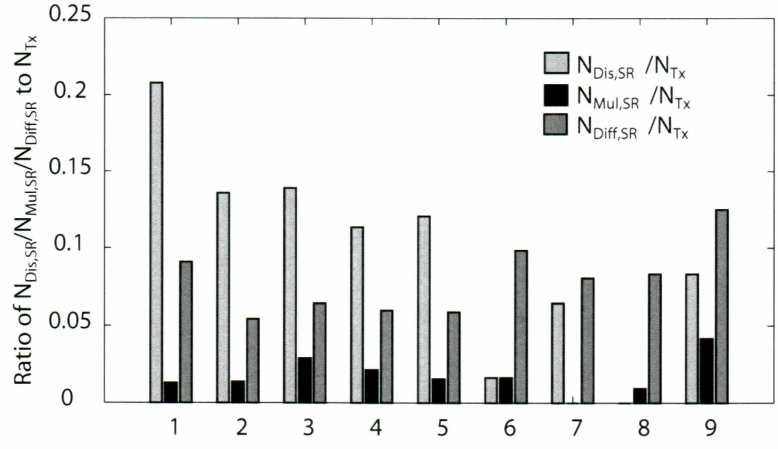

Figure 2.28. Occurrence rate in percentage of the discrete, multipath and diffuse SR-WM echoes considering Kp from previous 24 hrs

From the figures 2.29 and 2.30, discrete SR-WM echoes are observed ≈14%, multipath SR-WM echoes are observed ≈2%, and diffuse SR-WM echoes are observed ≈6% of the time.

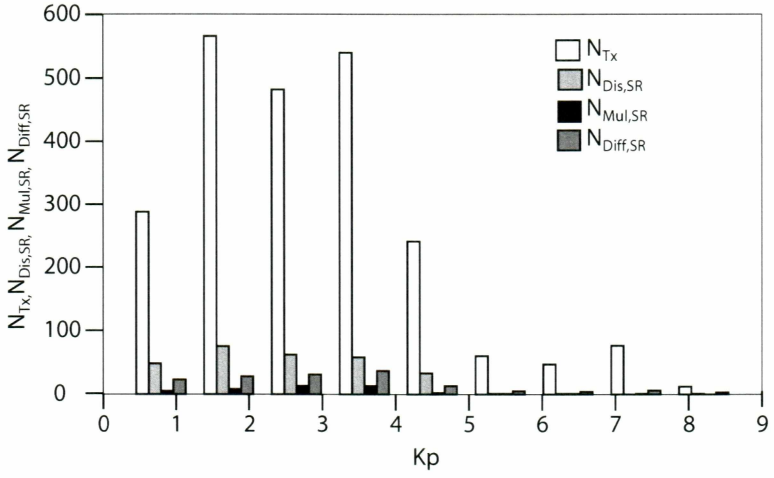

Figure 2.29. Histogram showing the numbers of program 38 transmissions and discrete, multipath and diffuse SR-WM echoes received on IMAGE as a function of $K_{p,max}$ in the previous 12 hours

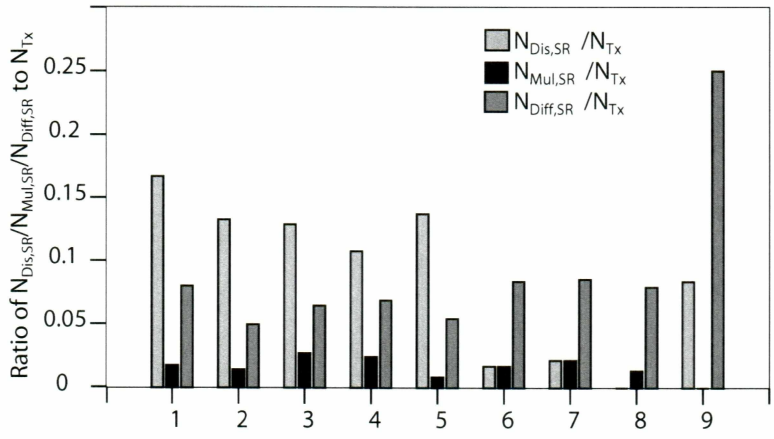

Figure 2.30. Occurrence rate in percentage of the discrete, multipath and diffuse SR-WM echoes considering Kp from previous 12 hrs

2.4 Conclusions

The occurrence patterns of WM echoes as a function of $K_{p,max}$ from previous 12 and 24 hours of the transmission time indicated that plasmagrams displaying any kind of WM echoes were observed ≈28% of the time. MR and SR-WM echoes were observed 18% and 20% of the time respectively. Discrete MR, multipath MR, and diffuse MR were observed ∼5%,<1%, and ∼14% of the time respectively. Discrete SR, multipath SR, and diffuse SR were observed ∼14%,<2%, and ∼7% of the time respectively.

The above statistics are based on the transmissions made at altitudes less than 5,000 km but discrete, multipath SR and discrete MR-WM echoes were observed more commonly inside the plasmasphere. Diffuse SR-WM echoes were observed more commonly at the high latitude region and at altitudes less than 2,500 km. If the transmissions made only at these latitudes were considered then the rate of occurrence of these echoes would more than double. IMAGE spends about half an hour in the high latitude region and about one and a half hours at altitudes less than 5,000 km. Therefore, the number of transmissions made at high latitudes is one-third of the total number of transmissions made at low altitudes. This implies that the occurrence rate of diffuse SR-WM may be more than 14%. Similarly, occurrence rates of discrete, multipath SR and discrete MR-WM will be approximately 1.3 times the value obtained from this survey.

Chapter 3 WM echoes observed during quiet and stormy periods: Case studies

The objective of this chapter is to 1) study the lower part of the magnetosphere 1000-5000 km during quiet and disturbed periods using WM echoes observed by RPI/IMAGE, 2) to study the signatures of solar wind parameters during quiet and storm times, and 3) to study how WM echoing processes are effected during quiet and disturbed periods.

This chapter is organized into four sections. The first section of this chapter describes the variation of geomagnetic activity during the years 2004 and 2005. Geomagnetically quiet and disturbed periods are also identified. The second section describes the variation of solar wind parameters during quiet and disturbed periods. The third section discusses the occurrence patterns of a variety of WM echoes during quiet and disturbed periods. The last section presents the conclusions of this chapter.

3.1 Geomagnetic activity during 2004 and 2005: Identification of case studies

Solar activity determines the weather in the upper atmosphere. Kp and Dst are the geomagnetic indices that indicate the geomagnetic activity in the upper atmosphere.

Figures 3.1 and 3.2 show the plot of Kp every three hours and hourly Dst for the years 2004 and 2005, respectively. Kp can take values between 0 to 9. Kp values of 0-2 indicate that the magnetosphere is relatively quiet, 2<Kp<5 indicates a moderate geomagnetic activity, 5<Kp<6 indicates a minor storm, and Kp>6 indicates a major storm; as Kp increases the severity of the storm increases. Dst provides a quantitative measure of geomagnetic disturbance. During quiet periods the Dst value typically varies between -20

to 20 nT. Dst values of -20 and -50 nT indicate moderate conditions in the magnetosphere, -100 nT<Dst<-50 nT indicates a minor geomagnetic storm, and Dst<-100 nT indicates a major storm. During a typical geomagnetic storm, the level of Dst remains above its typical value for a period of 2-3 hours, this is called the onset of the storm. This is followed by a sudden decrease in the value of Dst, which is called the development of the main phase of the storm. The magnitude decrease represents the severity of disturbance. It takes around 12 days of time for Dst to get back to its typical value, which is the recovery period of the storm. In 2004, there were 6 major geomagnetic storms and out of those there was an extreme case where Dst went below -350 nT and Kp went above 8.5. In 2005, there were 9 major geomagnetic storms, out of which 2 were severe with Dst going below -200 nT and a Kp index of 8. It can be observed from Figures 3.1 and 3.2 that the magnetospheric conditions are quite variable and 2004 is relatively quiet compared to 2005.

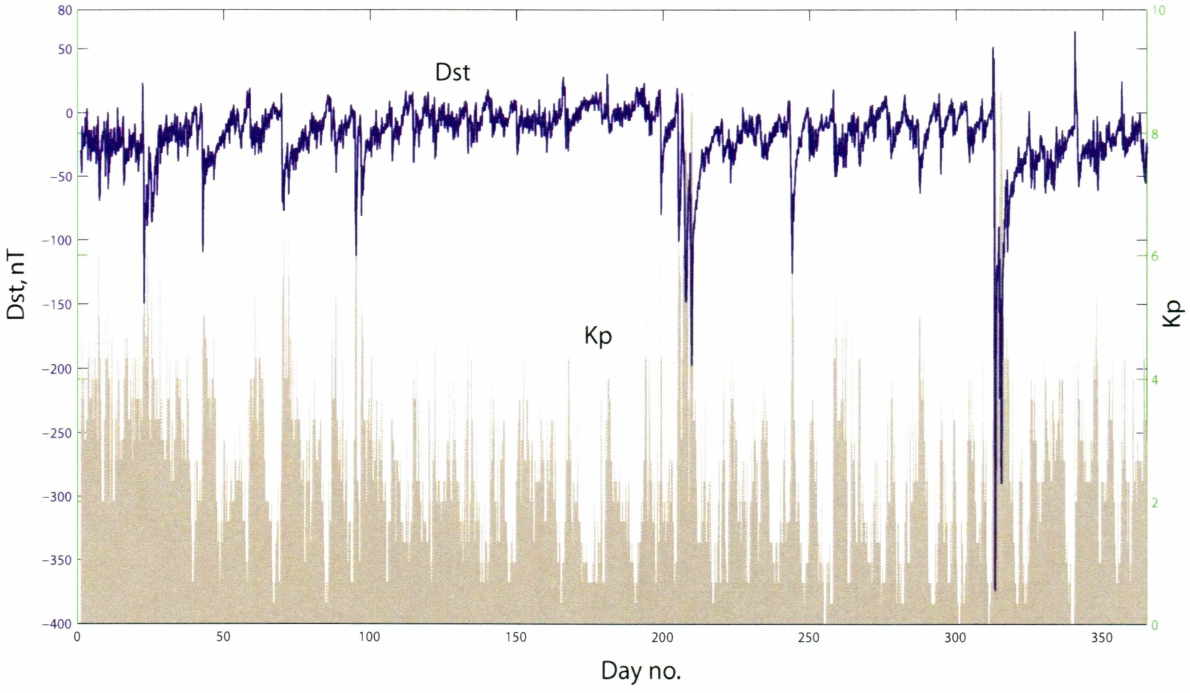

Figure 3.1. Variation of Kp and Dst in 2004. The left Y-axis is Dst, right Y-axis is Kp. X-axis is the day number. The blue curve represents Dst and the grey colored histogram represents the Kp

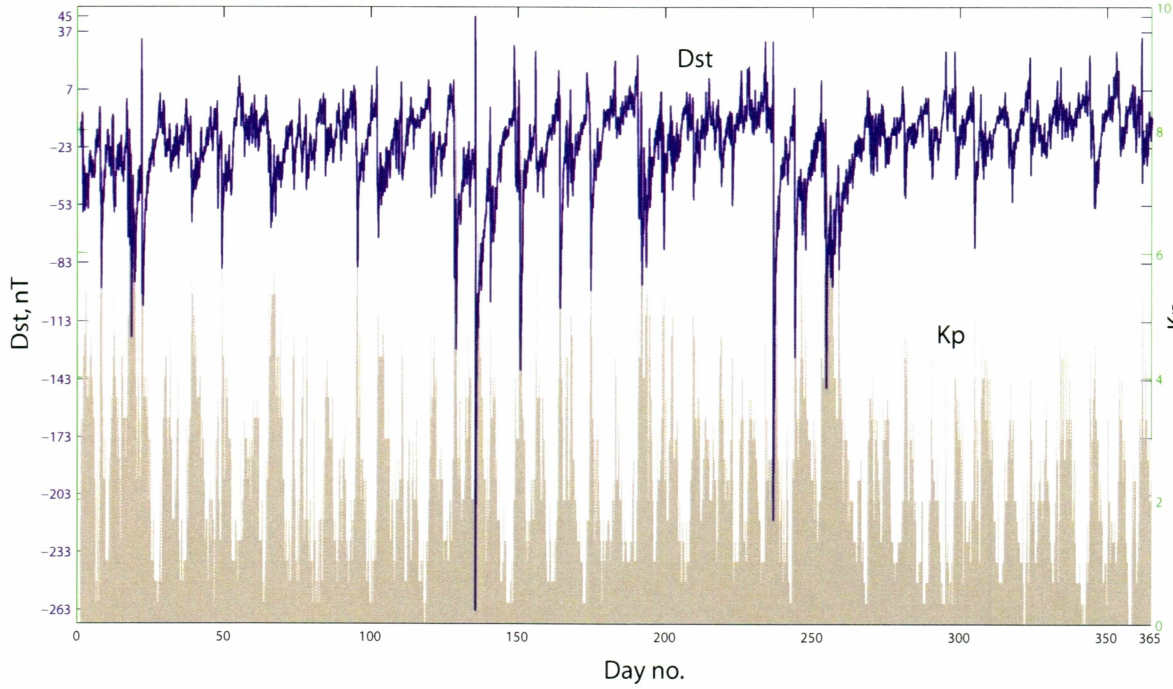

Figure 3.2. Variation of Kp and Dst in 2005. The left Y-axis is Dst, right Y-axis is Kp. X axis is the day number. The blue curve represents Dst and the grey colored histogram represents the Kp

In order to relate WM echoes to geomagnetic activity we need to choose the periods where there are sufficient transmissions of programs capable of seeing WM echoes. Program 38, whose frequency ranges from 6-63 kHz, was transmitted in the years 2004 and 2005, but only 138 transmissions of program 38 were made between January 2004 and August 2005. During the period of August-December 2005, 12 transmissions of program 38 were made at altitudes <5,000 km on almost every IMAGE orbit. Therefore, for our case studies we chose the August-December 2005 period. In this period we had major geomagnetic storms on Aug 24, on Sep 1 and on Sep 11 while relatively quiet geomagnetic conditions prevailed during the periods of Aug 17-Aug 23 and Nov 30-Dec 14.

The next section presents the occurrence pattern of WM echoes as a function of geomagnetic activity specific to the case studies selected.

3.2 The solar wind parameters and geomagnetic activity during case study periods

Figures 3.3 to 3.5 show the signatures of solar wind parameters measured by the WIND spacecraft, solar flux recorded by Solar Radio Monitoring Programme operated jointly by the National Research Council and the Canadian Space Agency, as well as Kp and Dst for the selected case studies.

According to both Kp and Dst, the geomagnetic conditions were relatively quiet to moderate during the periods Nov 30-Dec 14 (334-348; figure 3.3a) and Aug 17-Aug 23 (229-235; Figure 3.4a), and there were three geomagnetic storms during the period of Aug 24-Sep 24 (236-268; Figures 3.4a and 3.5a). This period also includes the recovery period of the three geomagnetic storms.

Solar flux is an indicator of solar activity and is used to determine the radiation being received from the sun. It is the amount of radio noise or flux that is emitted at a frequency of 2,800 MHz (10.7 cm wavelength). Solar flux can vary from 50 to 600 s.f.u. During quiet periods the average value of solar flux is around 100 s.f.u and it may rise up to a value of 600 s.f.u when there is a geomagnetic storm. For example, during the quiet period of

Nov 30-Dec 14, as shown in Figure 3.3b, on average the value of solar flux was ≈100 s.f.u and during the period of Aug 17-Sep 04, there was a sudden increase (4-4.5 times of its typical value) in solar flux during the days Aug 22 (234) and Aug 23 (235). A similar increase (6-6.5 times the typical value; Figure 3.4b) was also seen in the period Sep 06-Sep 24, on days Sep 10 (253) and Sep 11 (254). On Sep 14, solar flux increased to 300. There was also a geomagnetic storm on Sep 1 but no increase in solar flux was measured. There was an increase in the solar flux from 100 to 300 on Sep 14 (257; Figure 3.5b) and a substorm according to Dst, or a storm according to Kp, was noticed on Sep 16 (259). These observations suggest that whenever there is an increase in the solar flux value, a geomagnetic storm may follow. However, it appears that geomagnetic storms also occur independently of solar flux.

Solar disturbances affect the Earth not only from changes in the intensity of radiation, but also through the solar wind - a gas of ionized, charged particles streaming away from the sun. Typically the speed of solar wind varies between 300-700 km/s but occasionally it can increase to 800 km/s or greater when there is a geomagnetic storm. For example, the speed of solar wind varied smoothly between 300-700 km/s during the quiet and moderate periods (Figure 3.3c), but the variation is not smooth during the disturbed period of Aug 22-Aug 26 (234-238) and there was a sudden increase in speed from 400 km/s to 700 km/s (figure 3.4c). A similar kind of abrupt variation in solar wind speed was also observed during the period of Sep 1 to Sep 4 (244-248). In figure 3.5c, there is a data gap on day 255, and the speed of the solar wind increases up to 1000 km/s [$http://cdaweb.gsfc.nasa.gov/cdaweb/istp_public/$]. Solar wind speed increased by almost three times (300-1000 km/s) during Sep 08-Sep 14 (252-258; Figure 3.5c). These different signatures of solar wind speed are possible indicators of geomagnetic storms.

Solar wind is tenuous, containing only a few particles per cubic centimeter, mainly protons and electrons. The density of these particles is typically 10-20 per cc but occasionally, when there is a storm, the density can go as high as 60 per cc. For example, during the quiet period of Nov 30-Dec 14 (Figure 3.3d), the proton density was 5 per cc but there was a

gradual increase in proton density during the period Dec 08- Dec 14 (342-344; Figure 3.3d) and then the density dropped to 5 per cc. During the period Aug 17-Sep 04 (Figure 3.4d), there was an increase in the proton density on Aug 21 (233) from 5-40, and on Aug 24 from 5-50(236; the day when there was a geomagnetic storm), and on Aug 31-Sep 1 from 10-30 (243-244; onset of the geomagnetic storm on Sep 1). Similarly an increase in proton density during disturbed times can be noticed in Figure 3.5d during the period Sep 08-Sep 10. This implies that the rapid increase in the proton density could be a sign of an impending or approaching geomagnetic storm.

When a plasma is heated or an electron or ion beam is injected into plasma, substantial temperature differences develop between the electrons and ions and their distributions are also in non-equilibrium. Therefore, there will be a substantial increase in the thermal speed. For example, during the period Nov 30-Dec 14 (Figure 3.3e), the variation in thermal speed follows the variation in the proton density with some delay. There was an increase in proton density on Dec 08-Dec 14 and an increase in thermal speed on Dec 10-Dec 14. The typical value of thermal speed is less than 100 km/s and this value may increase up to 200 km/s when there is a geomagnetic storm. An increase in thermal speed from ≈50-200 km/s on Aug 24 (236; there was a geomagnetic storm on that day according to Kp and Dst) in Figure 3.4e and on Sep 12 (255) in Figure 3.5e an increase in thermal speed can also be noticed. Therefore, a sudden increase in thermal speed (greater than 100 km/s), which is related to temperature and the number of electrons in solar wind also might indicate a geomagnetic storm.

B_z is the z-component of the magnetic field vector. Negative events of B_z indicate a geomagnetic storm . The value of B_z typically ranges between -10 and 10 nT. This value may drop down to -20 nT when there is a geomagnetic storm. For example, during the quiet period (Figure 3.3f) the B_z component varied between -10 to 10 nT and longer durations of negative B_z were not observed. During the disturbed periods (Figures 3.4f and 3.5f) longer durations of negative B_z can be noticed on Aug 24 (236), Aug 31 (243) and on Sep 11 (254). The value of B_z went as low as ≈-15 nT on Aug 24, indicating that the storm was intense.

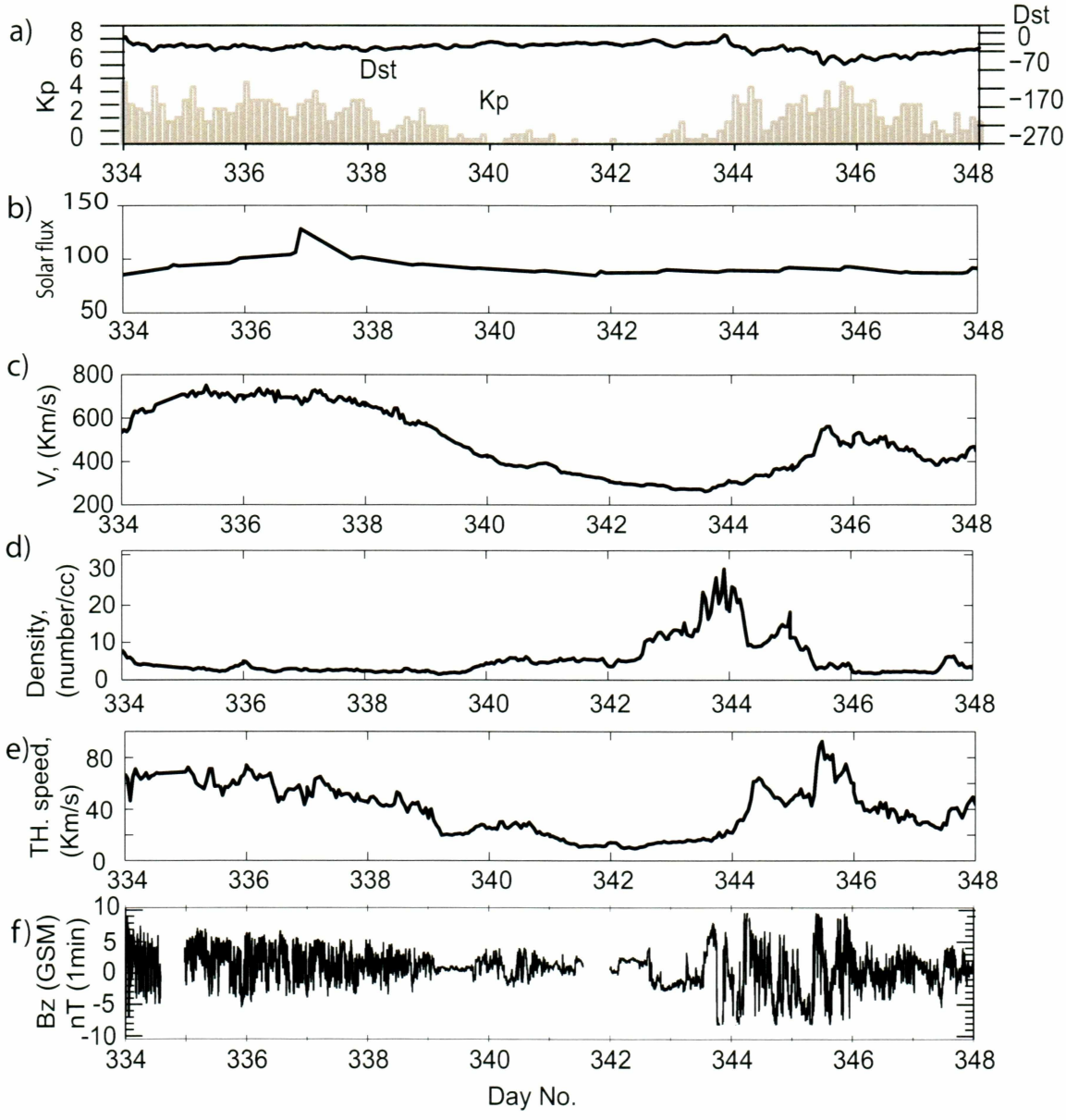

Figure 3.3. Variation of Kp and Dst (a), solar flux (Courtesy: Solar Radio Monitoring Programme operated jointly by the National Research Council and the Canadian Space Agency) (b), solar wind speed (c), proton density(d), proton thermal speed (e),and B_z component of IMF(f) measured by the WIND satellite , during the period 30 Nov-13 Dec 2005. Multipath MR-WM echoes were not observed during this period

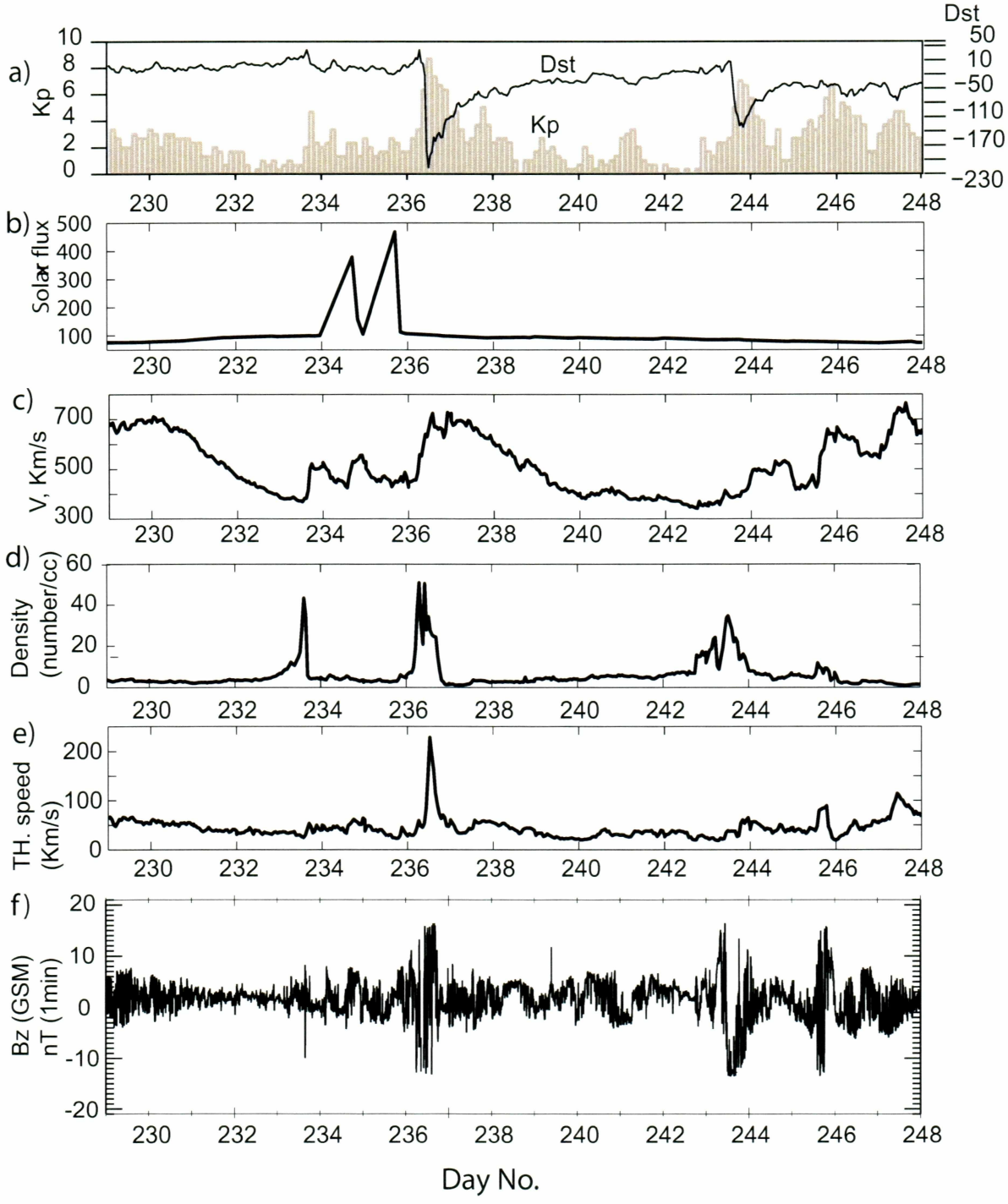

Figure 3.4. This figure has the same pattern as that of figure 3.3 but for the interval 17 Aug-04 Sep 2005

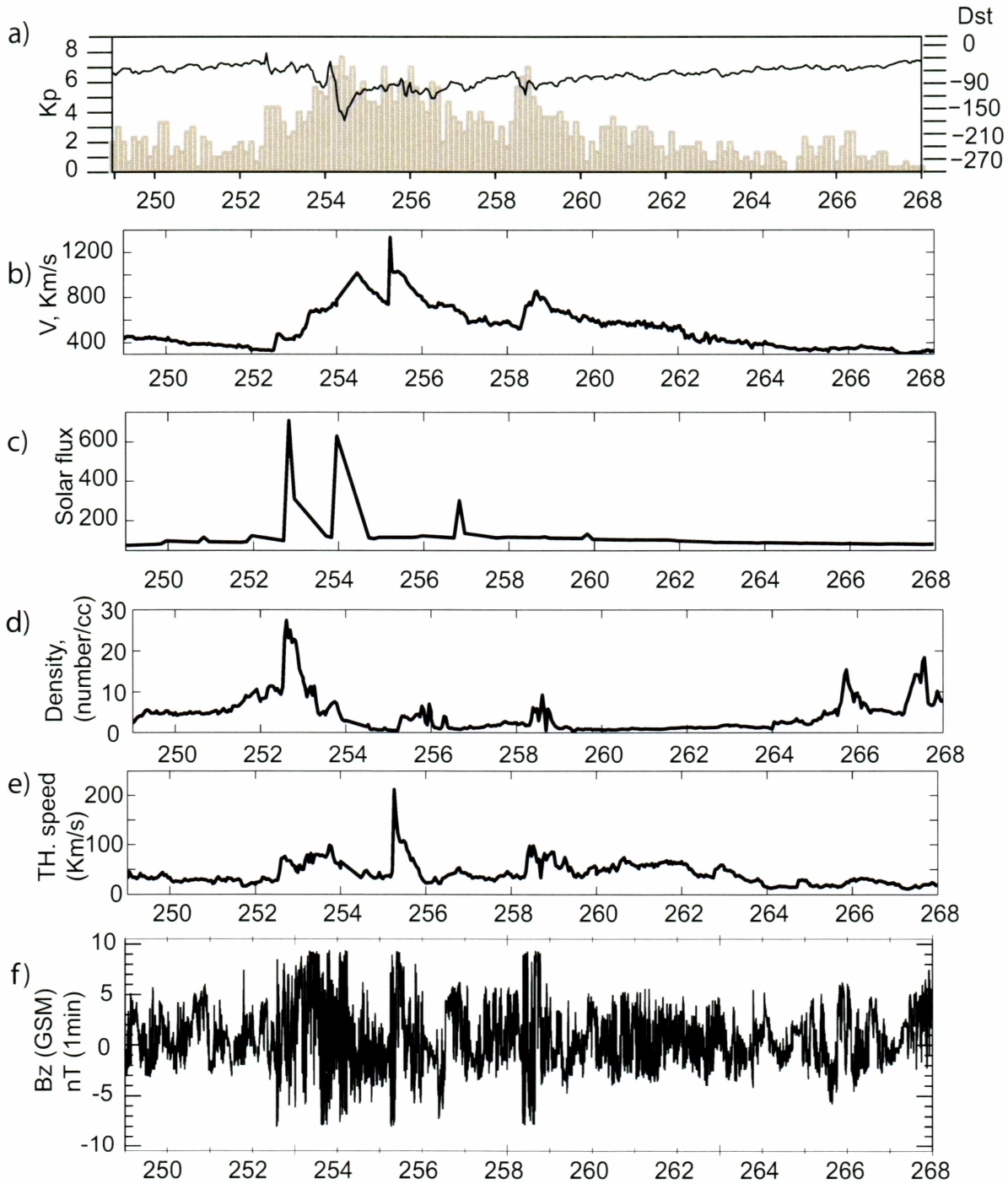

Figure 3.5. This figure has the same pattern as that of figure 3.3 but for the interval 05 Sep-24 Sep 2005

Signatures of various parameters indicating the solar activity and variations in earth's magnetic field suggest that there were three major storms during this period. The periods Nov 30-Dec 14 and Aug 17-Aug 23 were relatively quiet. Since Kp and Dst are the common indicators of geomagnetic storms, the next section discusses the occurrence patterns of SR- and MR-WM echoes as a function of Kp and Dst.

3.3 Occurrence pattern of MR- and SR-WM echoes during the case study periods

The IMAGE satellite travels around the earth in a 14.2 hour orbital period at different speeds when at different positions in the orbit. When the satellite is closer to the earth (i.e. near its perigee), its speed is much higher than when it is farther away or near its apogee. Because of the high speed near the perigee, the satellite crosses the low altitude region in $\approx$1 hr. Therefore, we have samples of WM activity for 1 hr every 14 hours.

Figures 3.6-3.8 show the occurrence pattern of WM echoes observed by RPI/IMAGE when program 38 was transmitted at altitudes less than 5,000 km during geomagnetically quiet and disturbed periods. In the three figures, the position of the vertical lines above the top x-axis indicate the time when the echoes were observed.

During the quiet period, 334-348, there were 22 IMAGE orbits and 263 transmissions of program 38 at altitudes less then 5,000 km and 55 cases of discrete SR, 2 cases of discrete MR, 16 cases of diffuse SR and 35 cases of diffuse MR were observed. During the period of Aug 17 (229) to Sep 04 (247) there were 7 geomagnetically quiet days (Aug 17 - Aug 23), and 12 geomagnetically disturbed days. There was a severe geomagnetic storm (Kp>8) on Aug 24 and another major geomagnetic storm on Aug 31. During the 7 geomagnetically quiet days there were 12 IMAGE orbits; there were 141 transmissions of program 38 and 18 cases of discrete SR, 6 cases of discrete MR, 6 cases of diffuse SR and 18 cases of diffuse MR were observed. During the 12 geomagnetically disturbed days (20 orbits) there were 237 transmissions of program 38 and 9 cases of discrete SR, 12 cases of discrete MR, 22 cases of diffuse SR and 26 cases of diffuse MR were observed. During the disturbed period

(249-268), there were 31 IMAGE orbits, 369 transmissions of program 38 were made, and 16 cases of discrete SR, 17 cases of discrete MR, 27 cases of diffuse SR, and 28 cases of diffuse MR were observed.

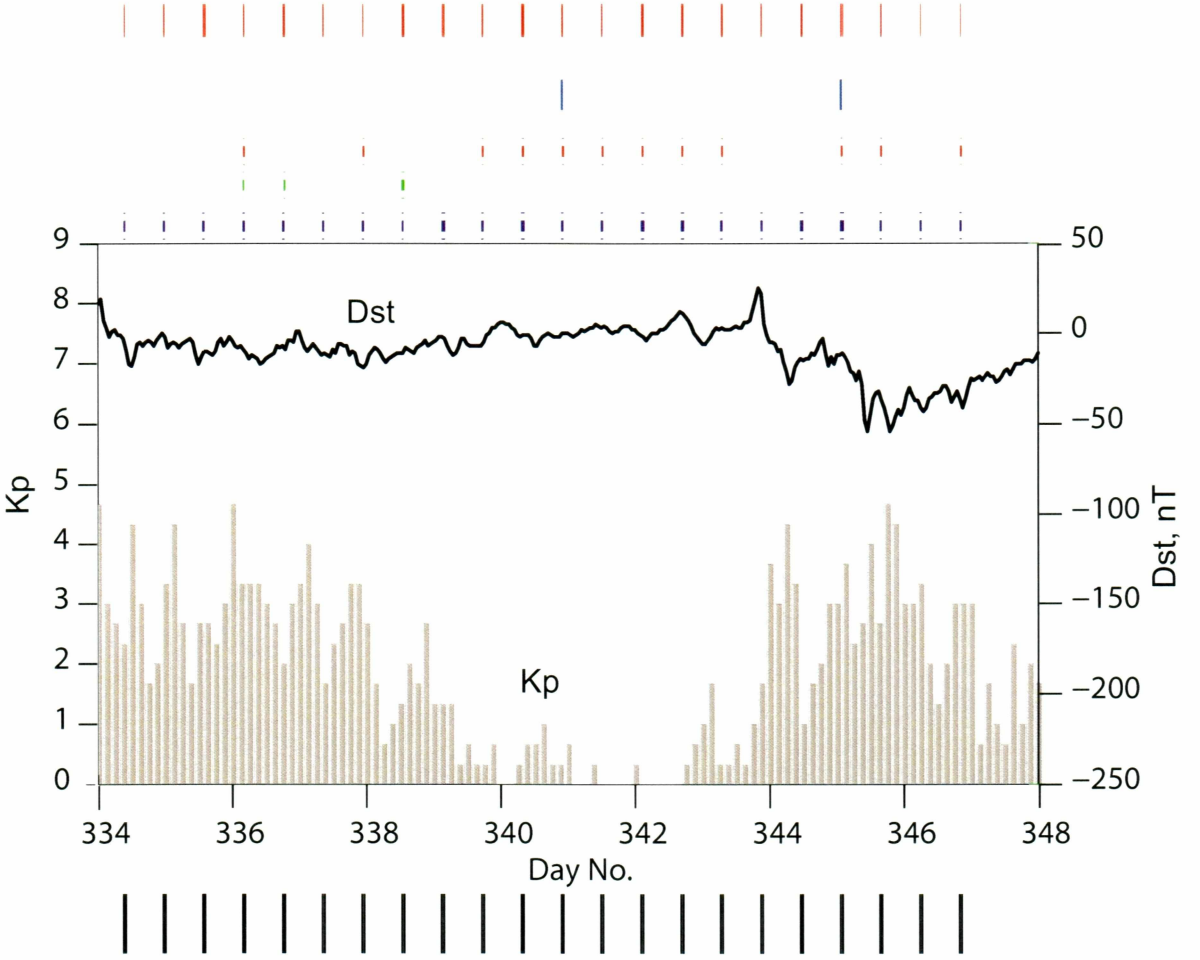

Figure 3.6. Occurrence of discrete MR (blue), multipath MR (green), diffuse MR (red), discrete SR (dashed blue), multipath SR (dashed green), and diffuse SR (dashed red) whistler mode echoes during geomagnetically quiet conditions. The thickness of these lines indicate the number of echoes observed. The black vertical lines on the bottom x-axis is the period of time when IMAGE is at low altitudes

Figures 3.9-3.11 show the IMAGE location when WM echoes (all kinds) were observed. Discrete SR-WM echoes (blue vertical dashed lines, Figures 3.6-3.8) were observed when IMAGE was at low latitudes, inside the plasmasphere and plasmapause region (shown in

Figures 3.9a, 3.10a and 3.11a). Multipath SR-WM echoes (green vertical dashed lines, Figures 3.6-3.8) were observed at all latitudes (Figures 3.9b, 3.10b and 3.11b). Diffuse SR-WM echoes (red vertical dashed lined, Figures 3.6-3.8) were observed more commonly at high latitude regions (polar regions, figures 3.9c, 3.10c and 3.11c). Discrete MR-WM echoes (blue vertical lines) were more commonly observed at low latitudes inside the plasmasphere (Figures 3.9d, 3.10d, and 3.11d). Multipath MR-WM echoes (green vertical lines) were observed at all latitudes (Figures 3.9e, 3.10e, and 3.11e). Diffuse MR-WM echoes (red vertical lines) were more commonly observed at low latitudes inside the plasmasphere during the quiet periods (figure 3.9f), but a relatively larger number of echoes were found at high latitudes during disturbed periods (figures 3.10f and 3.11f). Since Figure 3.10f includes the echoes observed during quiet (Aug 17-Aug 23) and disturbed periods (Aug 24-Sep 04) further analysis is needed to confirm that more diffuse MR-WM echoes are observed at the high latitude region during disturbed periods.

3.3.1 Occurrence pattern with respect to Dst:

According to Dst, the periods Nov 30-Dec 14 (334-348; Figure 3.6) and Aug 17-Aug 23 (229-235; Figure 3.7) were quiet (Dst>-20nT). Three geomagnetic storms were recorded during the period Aug 24-Sep 24 (236-268; Figures 3.7 and 3.8) beginning on Aug 24 (236), Aug 31 (243), and on Sep 11 (254). At the onset of the storm, Dst values are >0 for at least a couple of hours and then there is a large decrease in the value of Dst which is called as the main phase of the storm. The severity of the storm depends on the minimum value of Dst during the main phase of the storm. This phase lasts for a day or two and then it takes ≈12 days for the magnetosphere to recover from the storm. This period is called the recovery period. This is indicated by the magnitude of Dst stabilizing at ≈20 nT. For example, Dst was greater than zero on Aug 24 (236)and Aug 31 (243) before a large decrease in Dst was observed (Figure 3.7), which indicates the onset of the storm. Similarly, the onset of the storm recorded on Sep 11 occurred on Sep 09 (251; Dst>0). On Aug 24 the minimum value of Dst is -220 nT (Figure 3.7), on Sep 1 it is -140 nT (Figure 3.7) and on Sep 11 it is -160

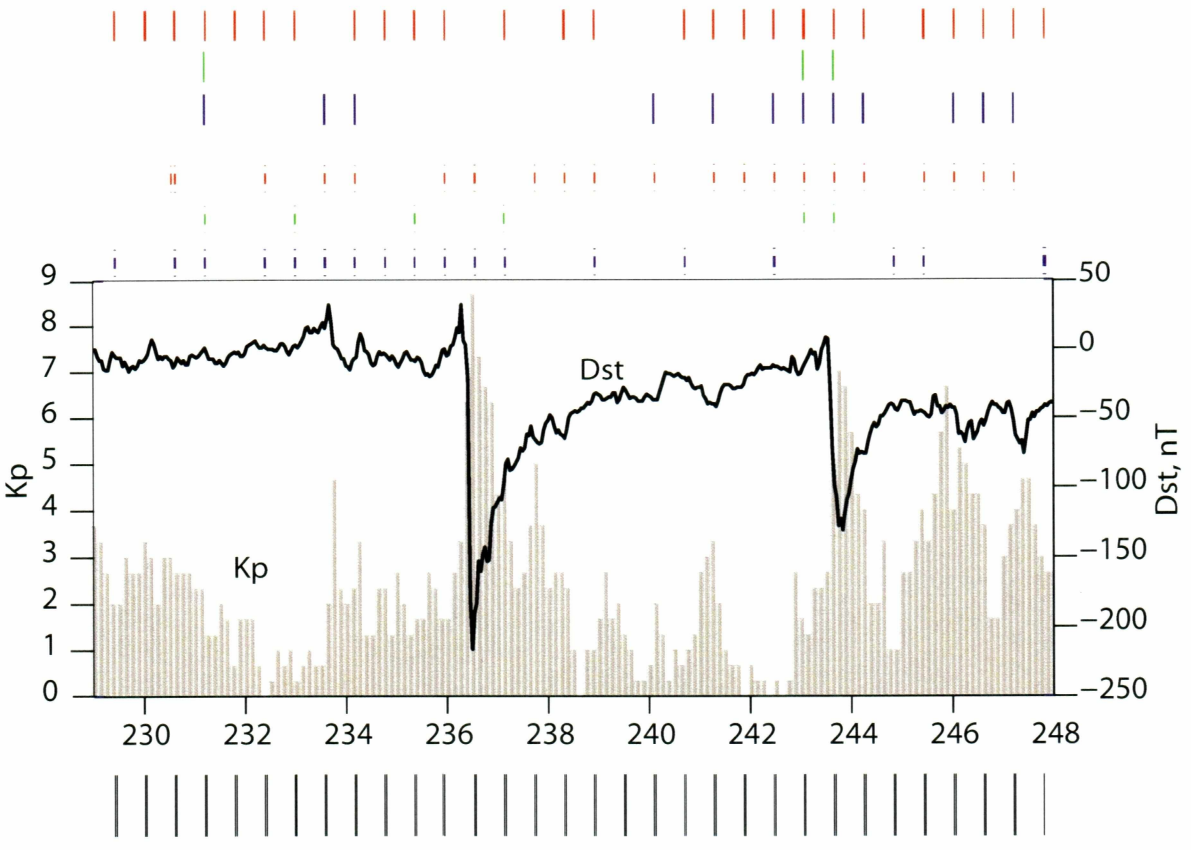

Figure 3.7. Occurrence pattern of WM echoes during the period Aug 17 (229) to Sep 04 (248). The pattern is same as that of figure 3.6

nT (Figure 3.8); this implies that the storm recorded on Aug 24 was severe compared to the other two storms. It can also be noticed from Figures 3.7 and 3.8 that the magnetosphere did not recover from the storm recorded on Aug 24 since there was only a 6 day gap between the two storms on Aug 24 and Aug 31. Similarly, there was only a 10 day gap between the storms on Aug 31 and Sep 11. Hence, the magnetosphere did not recover completely from the storm. It can be observed from Figure 3.8 that, by the end of the recovery period of the geomagnetic storm recorded on Sep 11, Dst is stabilized for a day or two at -20 nT, indicating complete recovery of the magnetosphere. In this subsection, the occurrence of SR and MR-WM echoes with respect to different phases of a storm as indicated by Dst are discussed.

During the quiet periods, there were 33 orbits of IMAGE, $\approx$215 transmissions of program 38 were made at low latitudes ($<60^{\circ}$), and 74 discrete SR-WM echoes (blue vertical dashes) were observed (i.e., discrete SR-WM echoes were observed $\approx$30% of the time during the quiet period). Six discrete SR-WM on 5 orbits of IMAGE were observed at the onset of the storms (Figure 3.7, Aug 24; Figure 3.8, Sep 09-11) but, during the recovery period of the storms, very few discrete SR-WM echoes were observed. There were 44 IMAGE orbits, 285 transmissions during these periods and only 22 echoes were observed (i.e., they are observed $\approx$8% of the time during the recovery period of the storm). But at the end of recovery period it can be noticed from Figure 3.8 that discrete SR-WM echoes were observed on every IMAGE orbit (Figure 3.8, 266-268).

Four multipath SR-WM echoes were observed in the quiet period of Nov 30-Dec 14 (334-348; Figure 3.6) and three were observed in the quiet period of Aug 17-Aug 23 (229-235; Figure 3.7). Two multipath SR-WM echoes were observed at the onset of the storms beginning on Aug 31 and Sep 09. Two multipath SR-WM echoes in the recovery period of the storm beginning on Aug 24, two in the recovery period of the storm beginning on Aug 31 and four during the recovery period of the storm beginning on Sep 11 were observed. Very few multipath SR-WM echoes were observed during both quiet and disturbed periods. Further study is needed to find the occurrence pattern of these echoes as a function of

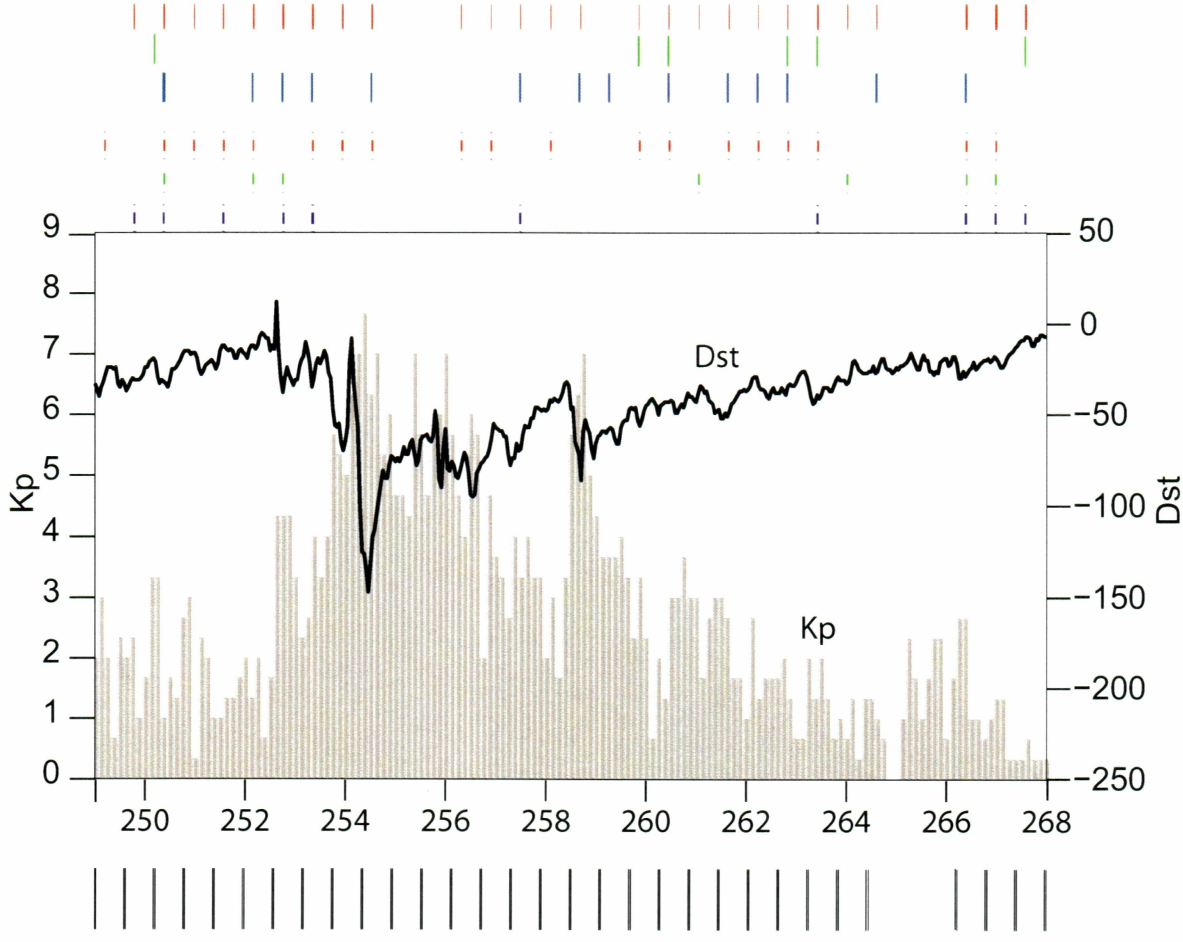

Figure 3.8. Occurrence pattern of WM echoes during the disturbed period Sep 06 (249) to Sep 24 (268). The pattern is same as that of figure 3.6

geomagnetic activity.

Diffuse SR-WM echoes (red vertical dashes) were observed on ≈50% of IMAGE orbits during the quiet periods. There were 165 transmissions in the high latitude region (>50°) during the quiet periods and 23 diffuse SR-WM echoes were observed (i.e., these echoes were observed ≈14% of the time). Diffuse SR-WM echoes were also observed during the onset of the three storms. Twelve diffuse SR-WM echoes were observed on 5 orbits and there were ≈25 transmissions in the high latitude region. They were more commonly observed during the recovery period of the storms . There were 44 IMAGE orbits during the recovery period, 220 transmissions were made at the high latitude region and 38 diffuse SR-WM echoes were observed (i.e., they were observed 17% of the time). These patterns imply that diffuse SR-WM echoes were observed during both quiet and disturbed periods (onset+recovery), but were more frequently observed during disturbed periods.

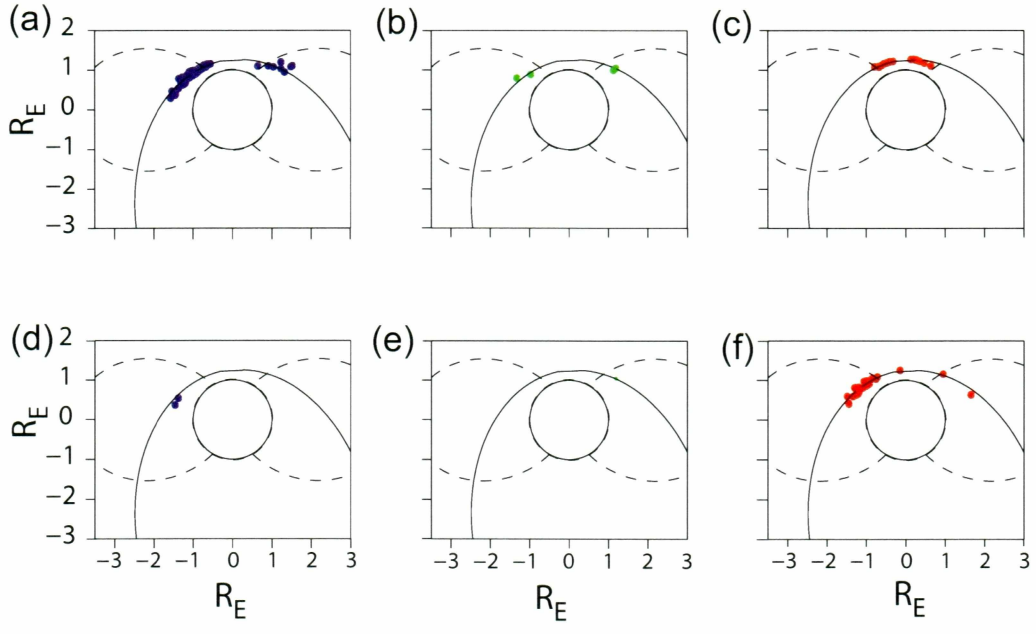

Figure 3.9. Low altitude portion of Dec 06 orbit is plotted. Location of IMAGE when a) discrete SR- b) multipath SR c) diffuse SR- d) discrete MR- e) multipath MR- and f) diffuse MR-WM echoes were observed during the quiet period Nov 30 (334)-Dec14 (348) when program 38 is transmitted at altitudes <5,000 km. L=4 is shown as reference

Four discrete MR-WM echoes (blue vertical lines) were observed during the quiet periods. There were 33 orbits during the quiet period but discrete MR-WM echoes were observed only on three orbits: one echo on each of the two orbits and two echoes on the third orbit (Figures 3.6 and 3.7). They were observed at the onset of the storms beginning on Sep 1 and Sep 11 (Figures 3.7 and 3.8). Five discrete MR-WM echoes were observed, approximately one echo per orbit at the onset of the storm. These echoes were more commonly observed in the later part of the recovery period (Figures 3.7 and 3.8). There were 285 transmissions (44 IMAGE orbits) inside the plasmasphere (L=4) and 23 discrete MR-WM echoes were observed during the recovery period. These patterns suggest that discrete MR-WM are more commonly observed when the magnetosphere is recovering from the geomagnetic storms than when the magnetosphere is relatively quiet.

One multipath MR-WM echo (green vertical lines) was observed during the quiet period Aug 17-Aug 23 (Figure 3.7) and no multipath echoes were observed during the quiet period of Nov 30-Dec 14 (Figure 3.6). A multipath MR-WM echo was observed at the onset of the storm beginning on Aug 31. Eight multipath MR-WM echoes were observed during the recovery period of the storm. These occurrence patterns suggest that multipath MR-WM echoes were more frequent during disturbed periods than in quiet periods. But very few echoes (9 in disturbed, 1 in quiet) were observed during both quiet and disturbed periods. Therefore, further study is needed to find the occurrence pattern of WM echoes as a function of geomagnetic activity.

Diffuse MR-WM echoes were most commonly observed during the quiet periods, when at least one diffuse MR-WM echo was observed on each IMAGE orbit. During this period there were 370 transmissions (33 IMAGE orbits) at altitudes <5,000 km and 52 diffuse MR-WM echoes were observed (i.e., 14% of the time). Diffuse MR-WM echoes were also observed at the onset of the storms beginning on Aug 31 and Sep 11; sixty transmissions (5 IMAGE orbits) were made and 8 diffuse MR-WM echoes were observed. However, during the recovery period of the storms they are often not observed; there were 505 transmissions at altitudes <5,000 km and 47 echoes were observed (i.e., 9% of the time). These occurrence

patterns suggest that diffuse MR-WM echoes were observed more frequently during quiet periods than during disturbed periods.

3.3.2 Occurrence pattern with respect to Kp:

According to Kp, the magnetosphere was quiet during the Dec 05-Dec 10 period (Figure 3.6; 339-344), moderate during the Nov 30-Dec 04, Dec 10-Dec 13, and Aug 17-Aug 23 (Figures 3.6 and 3.7; 334-338; 344-347; 229-235). There were five geomagnetic storms (Kp>6) during the Aug 24-Sep 24 period (236-268), beginning on Aug 24 (236), Aug 31 (244), Sep 03 (246), Sep 11 (254), and Sep 16 (259). During the period Sep 11-Sep 13 the kp value did not always exceed 6, which is considered as an indicator of major geomagnetic storm, as the value fluctuated between ≈4 and 8. However, as these fluctuations occurred within a relatively short span of time this will be considered a single storm beginning on Sep 11. A sudden rise in the Kp value (>6) is considered the beginning of the storm. Since the magnetosphere takes around 10-12 days to recover form the storm, the twelve day period after the beginning of the storm is also considered to be the disturbed period, although kp values fluctuate between 2-5 suggesting quiet and moderate geomagnetic conditions. This period is addressed as the recovery period in the text.

Discrete SR-WM echoes were more commonly observed during both quiet and moderate geomagnetic conditions. During 6 geomagnetically quiet days, there were 10 IMAGE orbits, ≈65 transmissions at low latitudes (<60°) and 33 discrete SR-WM echoes were observed (i.e., almost 50% of the time). During 17 geomagnetically moderate days (27 IMAGE orbits), there were 190 transmissions, and 39 discrete SR-WM echoes were observed (i.e., ≈20% of the time). These echoes were also observed at the beginning of the storms recorded on Aug 24 and Sep 03. Discrete SR-WM echoes were not often observed during the recovery period of the storm. During 30 geomagnetically disturbed days (including the day the storm was recorded; 49 IMAGE orbits), there were ≈ 310 transmissions and 28 discrete SR-WM echoes were observed (i.e., ≈9% of the time). However, these echoes were again observed frequently in the later part of the recovery period (266-268). In short, discrete SR-WM

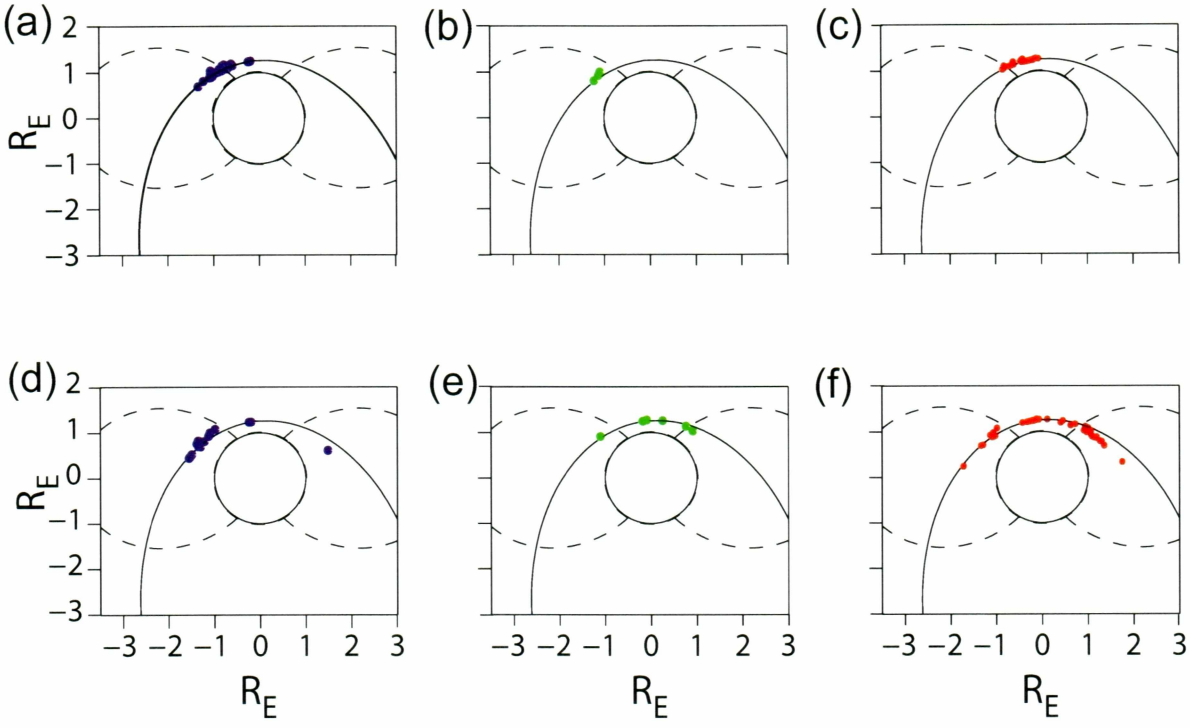

Figure 3.10. Low altitude portion of Aug 17 IMAGE satellite orbit is plotted.The format is same as that of figure 3.9 but for the interval 17 Aug-Sep 04, 2005

echoes were observed during quiet periods, moderate periods and at the onset of the storm but they were not often observed during recovery periods of the storm.

Multipath SR-WM echoes were not observed during the quiet period. Seven multipath SR-WM echoes were observed during moderate days when Kp was about 3. One multipath SR-WM echo was observed during the beginning of the storm recorded on Aug 31. Nine multipath SR-WM echoes were observed during the recovery periods of the storms. This implies that multipath echoes observed during disturbed and moderate geomagnetic conditions are comparable. But since only a few number of echoes were observed, further work needs to be done to find the occurrence patterns of multipath SR-WM echoes with respect to geomagnetic activity.

Diffuse SR-WM echoes were observed commonly during the quiet periods. During 6 geomagnetically quiet days there were $\approx$50 transmissions in the polar region and 11 diffuse SR-WM echoes were observed (i.e., $\approx$22% of the time). During moderate geomagnetic conditions (17 days, 27 IMAGE orbits), there were 135 transmissions, and 13 diffuse SR-WM echoes were observed (i.e., $\approx$9% of the time). These echoes were also observed at the beginning of the storms recorded on Aug 31, Sep 03, and Sep 11. During 30 geomagnetically disturbed days (including the day the storm was recorded; 49 IMAGE orbits), there were $\approx$ 245 transmissions and 50 diffuse SR-WM echoes were observed (i.e., $\approx$20% of the time). These patterns suggest that diffuse SR-WM echoes were common during quiet and disturbed conditions but less number of echoes were observed during moderate geomagnetic conditions.

One discrete MR-WM echoes was observed during the quiet period. During 17 days when Kp indicated moderate geomagnetic conditions, 162 transmissions were made inside the plasmasphere (L=4), and 6 discrete MR-WM echoes were observed (i.e., $\approx$4% of the time). These echoes were observed at the beginning of the storms recorded on Aug 31, Sep 03, Sep 11 and Sep 16. During 30 geomagnetically disturbed days (including the days storms were recorded; 49 IMAGE orbits), 294 transmissions were made and 28 discrete MR-WM echoes were observed (i.e., $\approx$10% of the time). These observations imply that a

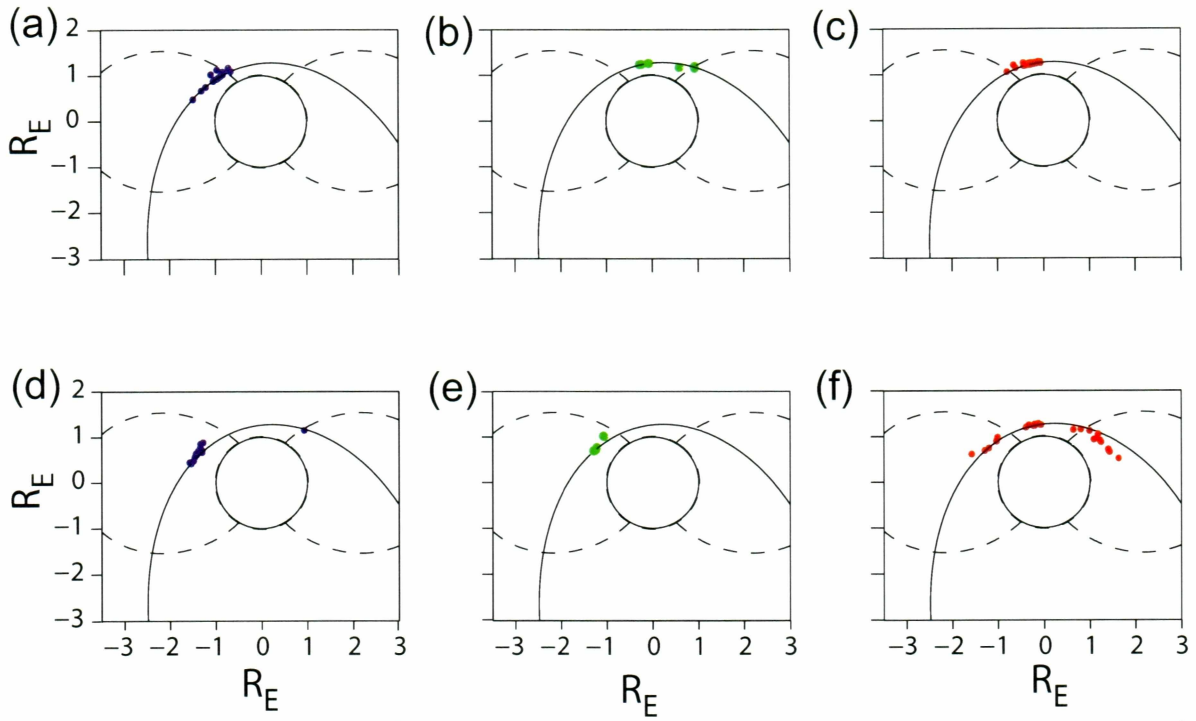

Figure 3.11. Low altitude portion of Sep 06 IMAGE satellite orbit is plotted.The format is same as that of figure 3.9 but for the interval 05 Sep-Sep 24, 2005

relatively higher number of discrete MR-WM echoes were observed during disturbed days.

Multipath MR-WM echoes were not observed during the quiet period. One multipath MR-WM echo was observed when there were geomagnetically moderate conditions. One multipath MR-WM echo was observed at the beginning of the storm recorded on Aug 31. During 30 geomagnetically disturbed days (including the days storms were recorded;) 9 multipath MR-WM echoes were observed. These statistics suggest that multipath MR-WM echoes were frequent during disturbed periods but since only a few echoes (<10) were observed, further work needs to be done to determine the occurrence patterns of multipath MR-WM echoes as a function of geomagnetic activity.

Diffuse MR-WM were more commonly observed during both quiet and moderate geomagnetic conditions. During 6 geomagnetically quiet days (10 IMAGE orbits), there were ≈105 transmissions made at altitudes less than 5,000 km and 20 diffuse MR-WM echoes were observed (i.e., ≈20% of the time). During moderate geomagnetic conditions (17 days, 27 IMAGE orbits), there were ≈300 transmissions, and 32 diffuse MR-WM echoes were observed (i.e., ≈11% of the time).These echoes were also observed at the beginning of the storms recorded on Aug 31, Sep 03, Sep 11, and Sep 16. During 30 geomagnetically disturbed days (including the days storms were recorded; 49 IMAGE orbits), ≈540 transmissions were made and 55 diffuse MR-WM echoes were observed (i.e., ≈10% of the time). These observations suggest that we see a relatively higher number of diffuse MR-WM echoes during quiet periods when compared to moderate or disturbed periods.

From the above occurrence patterns, it can be summarized that, according to both Kp and Dst, 1)discrete SR-WM echoes were observed >30% of the time during the quiet period and <10% of the time when the magnetosphere is disturbed; 2) Diffuse SR-WM echoes were observed in approximately comparable numbers, 14% and 17%, 22% and 20% of the time during the quiet and disturbed periods, according to Dst and Kp respectively; 3) discrete MR-WM echoes were observed <4% of the time during the quiet periods and >19% of the time during the disturbed periods; and 4) diffuse MR-WM were observed: a) ≈20% and ≈10% respectively according to Dst and Kp during the quiet periods b) ≈14% and ≈10%

respectively according to Dst and Kp during the disturbed periods.

From the above occurrence patterns it is suggested that the irregularities present at altitudes greater than 1,000 km ($f_{lh,max}$ altitude) during quiet periods affect frequencies below $f_{lh,max}$ and above $f_{lh,max}$ differently, thereby significantly affecting MR than SR-WM echoes. It is, however, interesting that the probability of discrete MR-WM has increased 4 times from quiet to disturbed periods. Since multipath WM echoes were observed during both moderate and disturbed geomagnetic conditions, we believe that long scale irregularities are present during both when geomagnetic conditions were moderate and disturbed. But further work is needed because we observed very few multipath WM echoes. These occurrence patterns of WM echoes also suggest that geomagnetic storms lead to significant enhancements in density structures (FAIs) at altitudes lower than 1000 km, thereby affecting primarily the propagation of SR-WM echoes that are reflected at ~90 km but not that of MR-WM echoes because they are reflected at altitudes > 1000 km.

3.3.3 VLF activity during quiet and disturbed periods

Figure 3.12 shows the variation in the natural VLF activity during the quiet and disturbed periods. Figure 3.12a shows a series dynamic spectra during the quiet period of November 30-December 12 (334-348; See Figure 3.6). Below the series of dynamic spectrograms is the plot of variation in Kp and Dst during that quiet period. To the right of this plot the low altitude portion of IMAGE orbit on 08 December 2005 is shown. Figure 3.12b shows a series dynamic spectra during the disturbed period of September 06-September 24 (249-268; See Figure 3.8). Below the series of dynamic spectrograms is the plot of variation in Kp and Dst during that disturbed period. To the right of this plot the low altitude portion of IMAGE orbit on 11 September 2005 is shown. VLF activity is the activity below f_{pe} and f_{ce}. The f_{uh} bands on the dynamic spectra gives a measure of f_{pe} (see Figure 2.7). The regions labeled 1,2,3, and 4 indicate VLF activity. The approximate locations of the satellite corresponding to the regions labeled 1, 2, 3, and 4 on the dynamic spectrograms are shown using red colored dots the IMAGE orbit plot. Regions 1 and 4 indicate the VLF

activity recorded when is IMAGE is at high altitudes greater than 30,000 km, regions 2 and 3 indicate VLF activity when IMAGE is in polar regions at altitudes less than 3,000 km.

In Figure 3.12a first panel shows the activity recorded during moderate geomagnetic conditions according to Kp. Second and third panels in Figure 3.12b shows the activity recorded during extremely quiet periods according to both Kp and Dst. Fourth panel shows the activity recorded during moderate geomagnetic conditions according to both Kp and Dst. In figure 3.12b first panel shows the activity recorded during the recovery period of the storm recorded on Aug 31 (Day 243; see Figure 3.7). Second panel in Figure 3.12b shows the activity recorded during the onset and main phase of the storm recorded on Sep 11. Third panel in Figure 3.12b shows the activity recorded when there is minor storm according to Kp and Dst and fourth panel shows the activity recorded during the recovery period of the storm.

A comparison of panels 2 and 3 of figure 3.12a with panels 1, 2, and 3 of figure 3.12b shows that there is an increase in the geomagnetic activity in region 1 and not much variation in the geomagnetic activity in regions 2, 3, and 4. We see enhanced AKR activity at high frequencies during disturbed periods when compared with quiet periods. Further work is needed to establish the relation between VLF activity and geomagnetic activity, VLF activity and the echoing process.

3.3.4 Variation of plasmapause during quiet and disturbed periods as calculated from Kp

Geomagnetic storms indicate that there is a disturbance in the earth's magnetic field. This also indicates that there is a change in the solar activity, solar wind speed, electron and ion density in the solar wind, and temperature of electron and protons. Apart from these, the electron density in the magnetosphere, ion composition, plasmapause location also change with a change in geomagnetic activity.

Figure 3.12 shows the plot of plasmapause L_{pp} locations as calculated from Kp (black dots) using the formula $L_{pp} = 0.56 - 0.46(K_{p,max})$ [Carpenter and Anderson, 1994]and

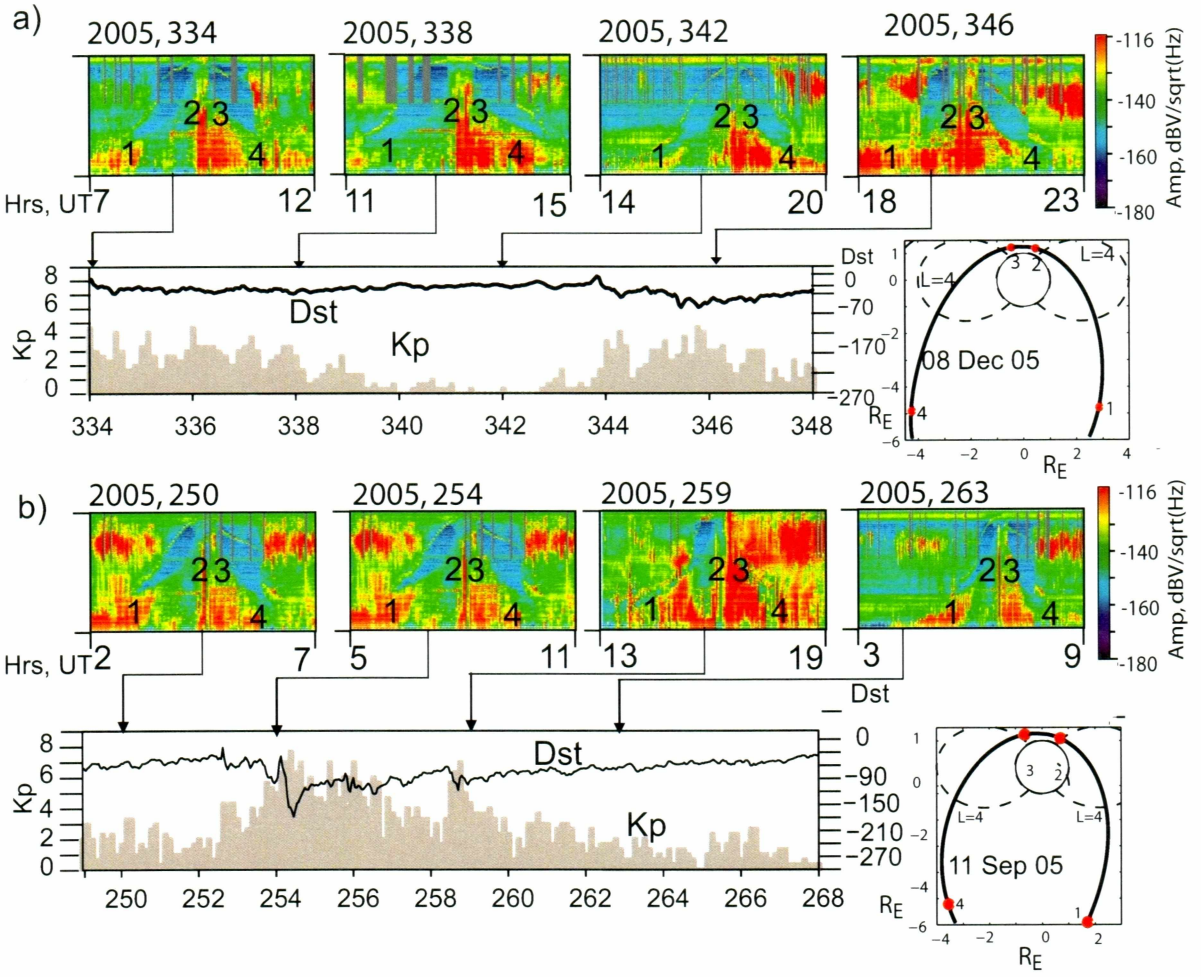

Figure 3.12. VLF activity during quiet (a) and disturbed periods (b)

from the sudden drop in f_{uh}, which can be observed on dynamic spectra. The IMAGE spacecraft carries an extreme ultraviolet (EUV) imager to detect solar EUV photons that are resonantly scattered by singly ionized helium in the plasmasphere. A sophisticated computer deconvolution technique is used to translate the EUV photon counts registered by the instrument into images of the plasmasphere. The images on the top x-axis in both top and bottom panels are the images of the plasmasphere taken by the EUV instrument on the IMAGE satellite. From both top and bottom panels it can be observed that the L_{pp} calculated from Kp and the L_{pp} calculated using f_{uh} measurements from dynamic spectra

agree well. During the disturbed period (top panel) L_{pp} varied between 2 and 8. There was a geomagnetic storm on Sep 11 (See Figure 3.8; day 254). A sudden drop in f_{uh} was not noticeable in the dynamic spectrograms during the main phase and initial phases of the recovery period. Therefore, L_{pp} measurements were not available. It can be seen that the plasmasphere merges during the main phase and the recovery periods of the storm, Sep 11-Sep 18 (254-261), and L_{pp} drops from 5 to 2. At the later part of the recovery period, Sep 19-Sep 24(262-268), L_{pp} expands and reaches a value of 5 according to Kp and >6 according to measurements from f_{uh}. During the quiet period (bottom panel) L_{pp} varied between L=4 to L=8. Geomagnetic conditions were extremely quiet (Kp<1) during the period Dec 06-Dec 10 (340-344) and were moderate (see Figure 3.6) during the periods Nov 30-Dec 05 (334-339) and Dec 11-Dec 13 (345-348). The plot suggests that, during extremely quiet periods, the plasmasphere expands from L=4 to L=8 and, during moderate geomagnetic periods, L_{pp} is approximately 4. It is interesting that during the extremely quiet period (day 341) f_{uh} measurements showed that L_{pp} values drops to 2 and on Dec 02 (343) the L_{pp} value increases up to 10. EUV images also show the evidence of plasmasphere expansion from moderate to quiet geomagnetic conditions. The observations of plasmapause locations suggest that the plasmasphere contracts during the disturbed periods, expands during extremely quiet periods, and L_{pp} $\sim$4 at moderate geomagnetic conditions.

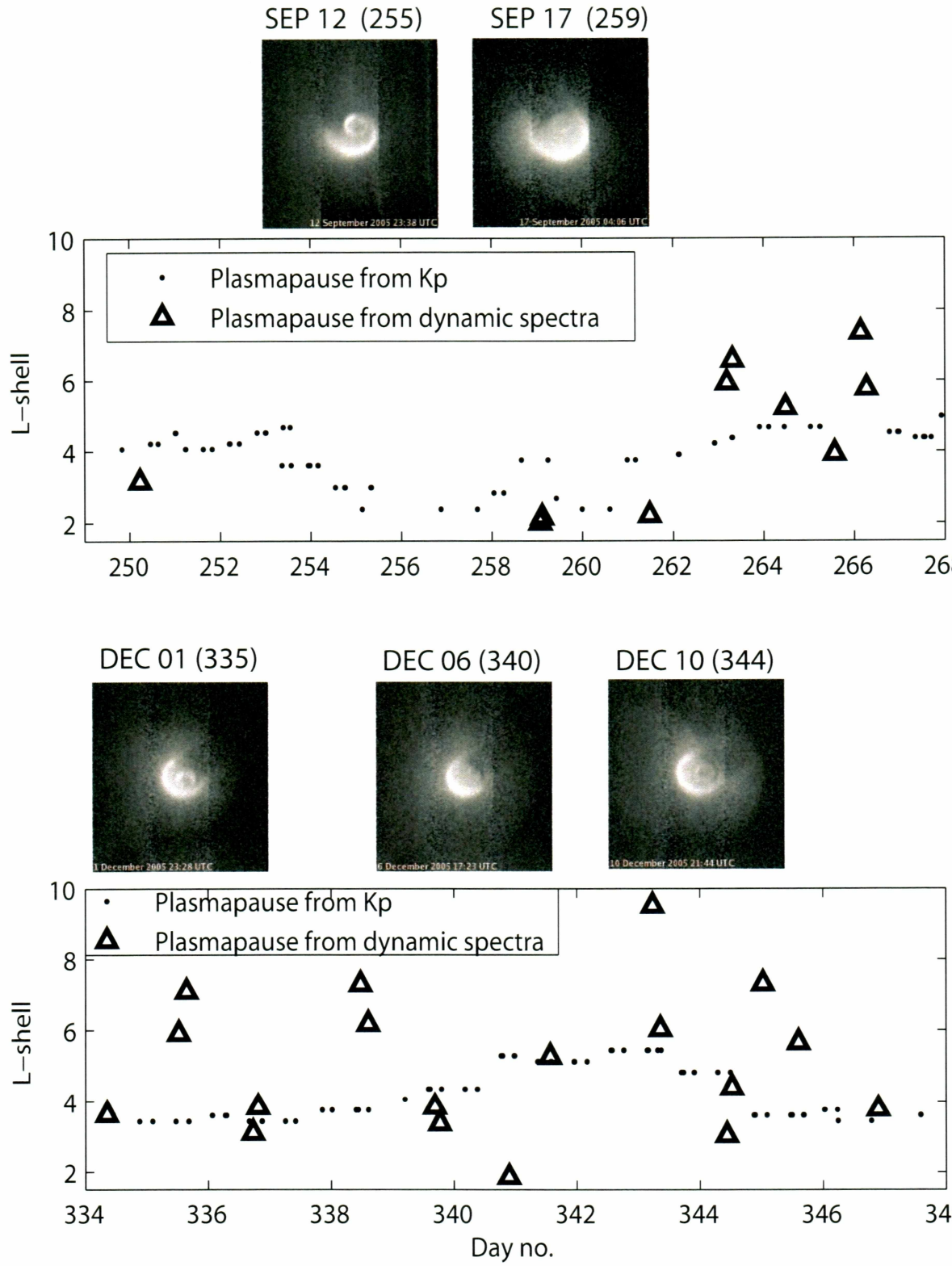

Figure 3.13. Plasmapause locations during quiet (bottom panel) and disturbed periods (top panel)

3.3.5 Electron Density measurements

The lower cutoff of MR-WM echo is the local lower hybrid frequency, f_{lh}. The lower hybrid frequency, f_{lh}, depends on f_{pe}, f_{ce}, and m_{eff}, the effective ion mass. Therefore, given f_{lh}, f_{ce}, and m_{eff}, the local electron density can be measured. Below is the formula from which the plasma frequency and, in turn, the local electron density can be calculated.

$$\frac{1}{1836 m_{eff}} \frac{1}{f_{lh}^2} = \frac{1}{f_{pe}^2} + \frac{1}{f_{ce}^2} \tag{3.1}$$

Figure 3.13 shows the plot plasma frequency (f_{pe}) as measured from the lower cutoff of MR-WM echo (f_{lh}) observed during both quiet and disturbed periods and gyro frequency (f_{ce}) calculated using IGRF model. The value of m_{eff} is assumed to be one in the calculations because, at higher altitudes, mostly H+ is present and the percentage of other ions is negligible.

It can be observed from figure 3.12c that the IMAGE orbit did not drift much during the four month period (Aug-Dec 2005). Therefore, using the lower cut off measure from the MR-WM, echoes electron density variations as a function of geomagnetic activity can be studied. Figure 3.13a shows the variation of f_{pe} as a function of L-shell and 3.13b shows the variation of f_{pe} as a function of altitude. The plasma frequency measured during quiet periods is indicated by red triangles and, during disturbed periods, is indicated by green circles. It can be observed from the plots that f_{pe} varies from 270-430 kHz (900-2,400 el/cc) during both quiet and disturbed periods. Although, there is no significant difference in the electron densities measured during quiet and disturbed periods, on an average the electron density measured during disturbed periods is less than that of quiet periods . Figure 3.13 b suggests that electron density is decreasing with an increase in altitude.

These observations suggest that electron density may not change significantly during quiet and disturbed periods. One possible reason could be that most of these echoes were observed inside the plasmasphere (L<4). More measurements at higher L-values may help

in developing a better understanding of these density variations at low altitudes.

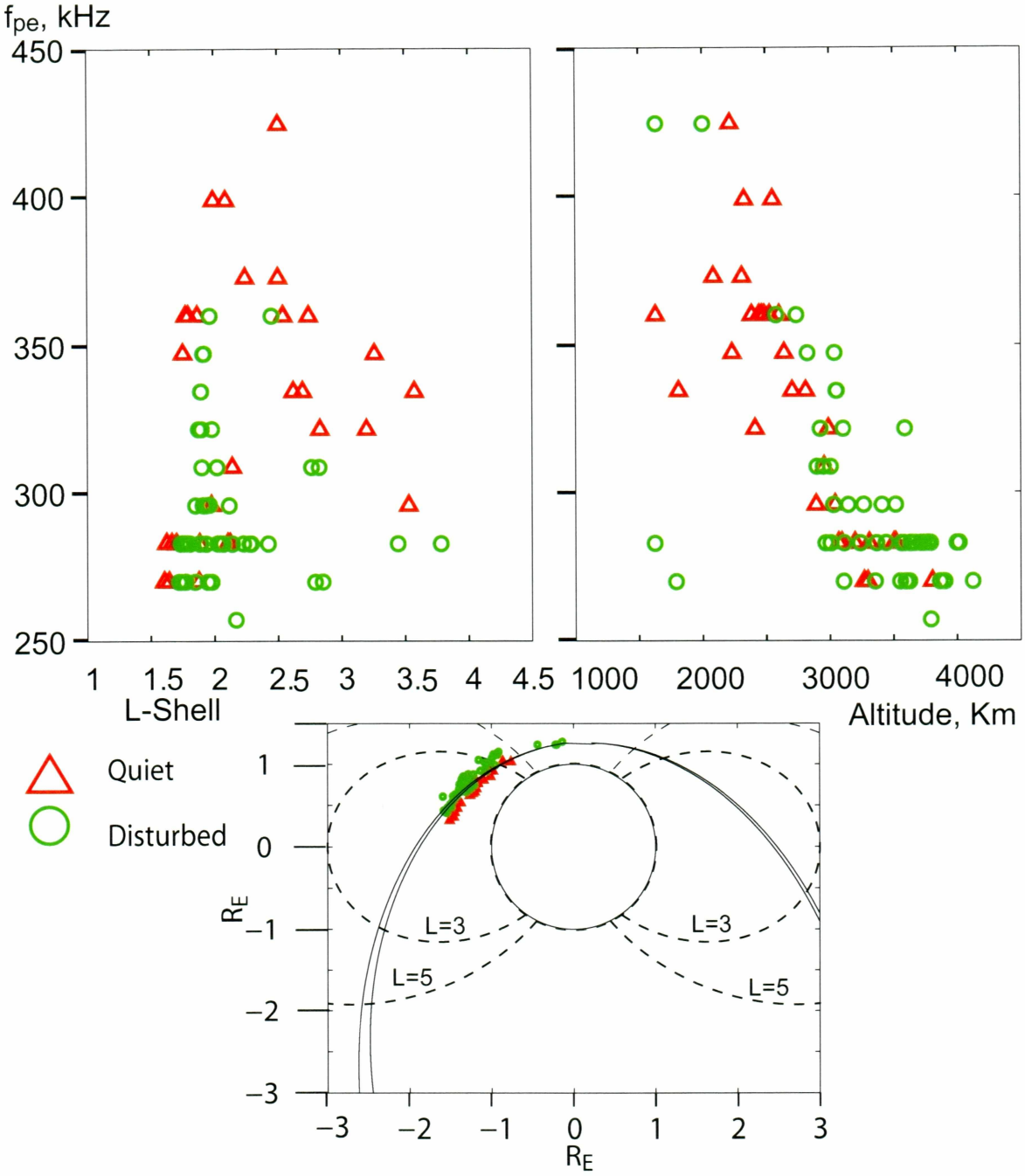

Figure 3.14. Plasma frequency measurements during quiet (red triangles) and disturbed periods (green circles)

3.3.6 Comparison with TEC data

The most fundamental parameter describing the ionosphere is electron number density, Ne (electrons/m^3). The line integral of Ne is termed Total Electron Content (electrons/m^2), or TEC. Tomographic images of the ionosphere are produced from TEC measurements made at a latitudinal chain of ground stations during flights of polar-orbiting satellites that transmit appropriate radio waves. TEC measurements can be used to study the variation in electron densities during quiet and disturbed periods at altitudes <800 km. These measurements can also be used to find the length scales of large scale irregularities at low altitudes.

Figure 3.14 shows the images developed from TEC measurements along many slant paths (3.14b) to the GPS receiving stations, Cordova, Gakona, Delta Junction, and Arctic village,AK on 24 August 2005. Figure 3.14a shows the locations of these GPS signal receiving stations. There were 6 TEC images on this day; the three images presented here are representative of all six images. There was a geomagnetic storm on 24 Aug 2005 (see Figure 3.7). On this day IMAGE was on HAARP (an hour before the TEC measurements were made) and the WM activity recorded by RPI is presented in figure 3.14c. The IMAGE satellite track is shown in figure 3.14a. This figure shows the observations of IMAGE on a disturbed day. There was a diffuse SR-WM echo observed at 13:13 UT at high latitudes (83°) and at 13:18 UT auroral hiss was observed at 68° latitude and at 13:22 UT we observed ground transmitter signals and a discrete SR-WM echo, also the frequencies below 25 kHz occupied the entire time delay range (4-170 ms). TEC images suggest that electron densities vary between $0.4 * 10^{11}$ to $3 * 10^{11}$ el/cc between 200-400 km altitude. We believe that these two data sets can be used to find the location, density enhancements, and scale sizes of small and large scale irregularities at latitudes less than 5,000 km.

Figure 3.15 shows the variation of electron density at low altitudes using TEC measurements on a geomagnetically quiet day and on a geomagnetically disturbed day. From Figure 3.6 we know that Dec 08, 2005 (342) is a geomagnetically quiet day with respect to both Kp and Dst. There was geomagnetic storm on Sep 11, 2005 (253) (see Figure 3.8). Six images of TEC were made on this day and the images shown here are representative of

all six images. TEC measurements show that, during quiet periods electron densities varied between $0.2 * 10^{11} - 0.6 * 10^{11}$ el/cc between 0231-0252 and 1458-1518UT. An increase in the electron density to $1.2 * 10^{11}$ el/cc was observed at 2001-2021 UT. During disturbed periods significant enhancements in the electron densities were observed. Electron density increased up to $6 * 10^{11}$ el/cc. These observations suggest that there is an increase in electron densities in the low altitude region of the ionosphere and the variation of long scale irregularities scale sizes could be studied.

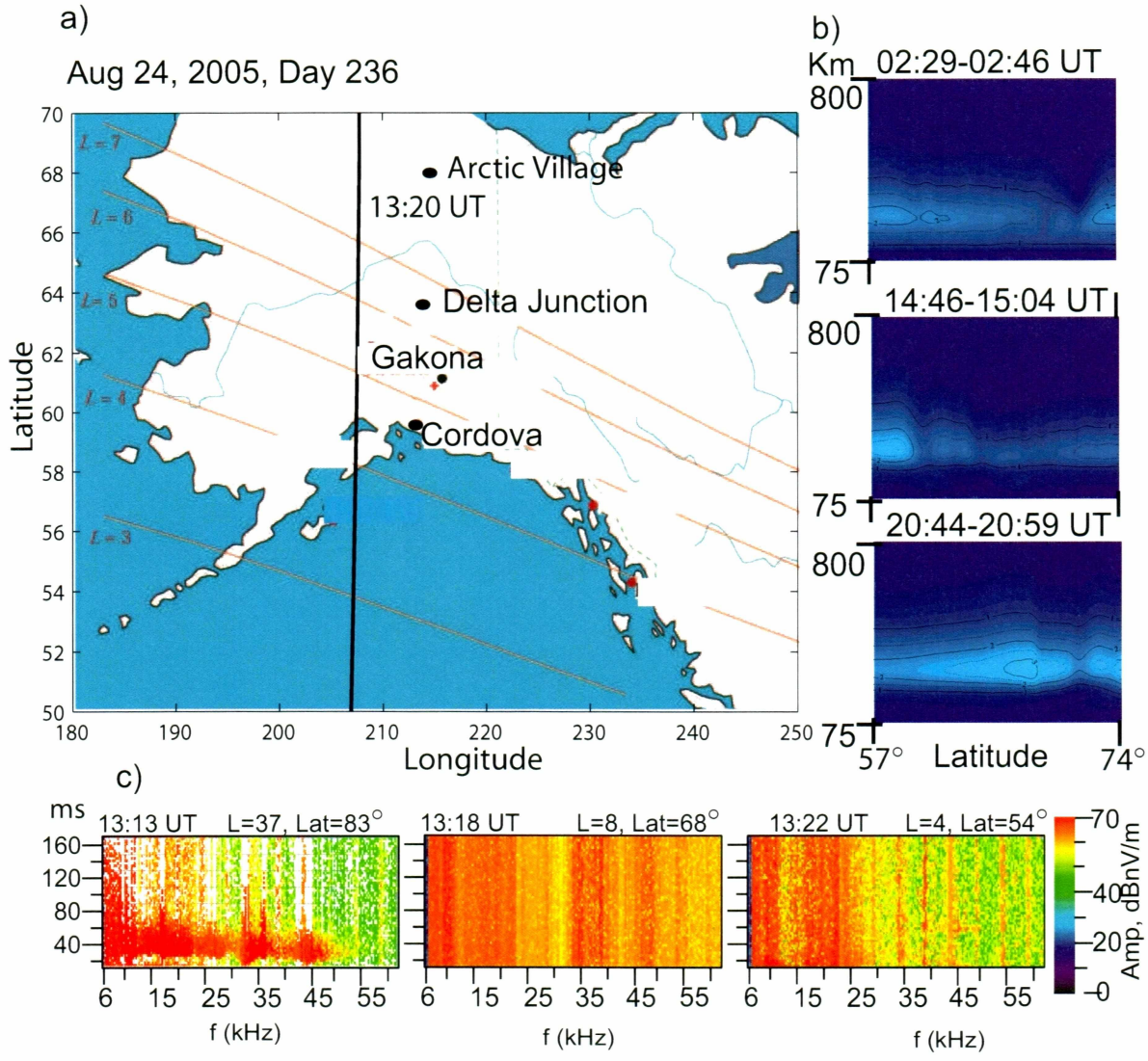

Figure 3.15. IMAGE sateliite tracks (a), Images of TEC (b), WM data recorded by RPI/IMAGE (c) on 24 August 2005

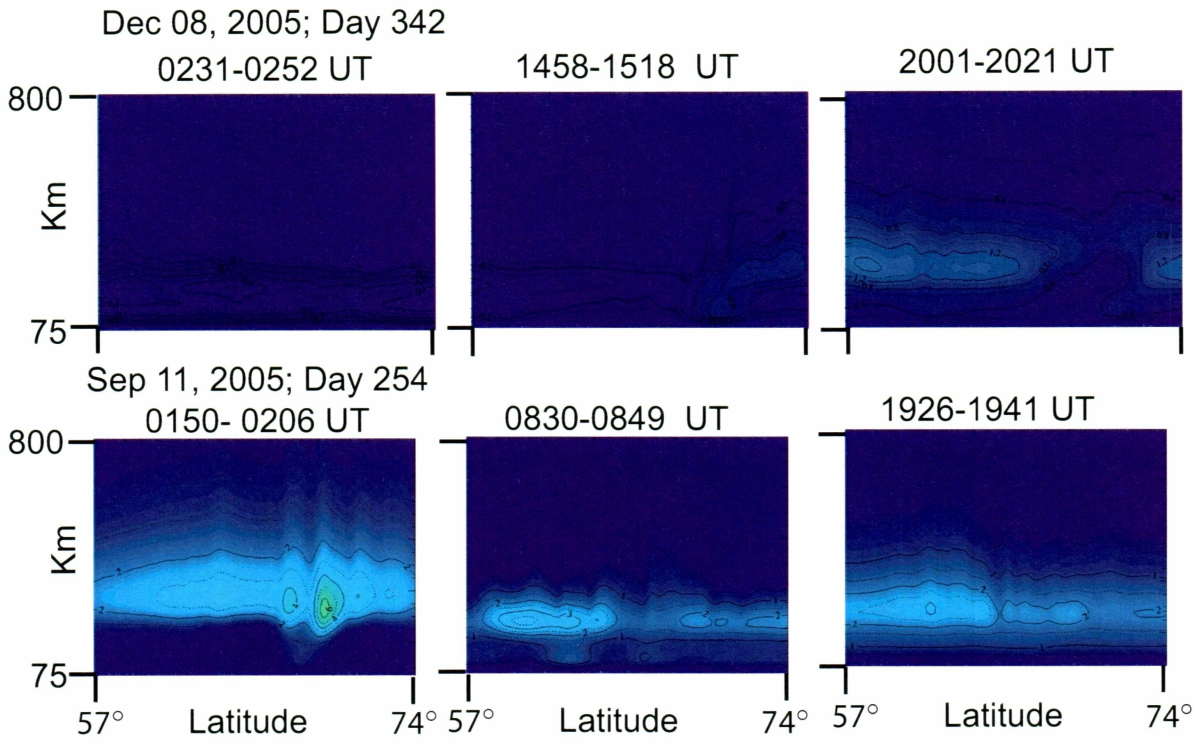

Figure 3.16. Measurements of TEC on geomagnetically quiet (Dec 08, 2005; top panel) and disturbed (Sep 11, 2005; bottom panel) day

3.4 Conclusions

Based on the results of chapter 3, we believe that there may not be a significant variation in the electron density during quiet and disturbed periods but geomagnetic storms may lead to significant enhancements in density structures (FAIs) at altitudes lower than 1000 km, thereby affecting primarily the propagation of SR-WM echoes that are reflected at ~90 km but not that of MR-WM echoes because they are reflected at altitudes > 1000 km. A possible explanation for not seeing relatively more numbers of diffuse SR-WM echoes during disturbed periods could be low RPI signal strength. Even though WM waves undergo forward scattering at higher altitudes, they may not have enough strength to come back to the satellite. Density structures present at altitudes >1,000 km significantly affect frequencies below $f_{lh,max}$ during quiet and moderate geomagnetic conditions. Therefore we see diffuse MR-WM echoes during both quiet and moderate geomagnetic conditions but not diffuse SR-WM echoes. However, it is surprising that we see a significantly lower number (one-fifth) of discrete MR-WM echoes during quiet periods.

Chapter 4 Summary and recommendations for future work

In this chapter, we conclude the thesis by providing the summary and recommendations for future work.

4.1 Summary

A data survey for WM echoes observed by RPI/IMAGE during the period Jan 2004-Dec 2005 when program 38 was transmitted at altitudes <5,000 km has been performed. Examples of the variety of WM echoes observed on IMAGE and their generation mechanisms were presented. The occurrence patterns of discrete, multipath, and diffuse, MR- and SR-WM echoes were discussed.

1. Discrete and multipath SR-WM echoes were observed at low latitudes (<60°) including the plasmasphere and plasmapause region and at altitudes <5,000 km. Diffuse SR-WM echoes were observed in high latitude region (>50°) and at altitudes <2,500 km. These results are consistent with Sonwalkar et al. [2004].

2. Discrete MR-WM echoes were observed at low latitudes (<60°) including the plasmasphere and plasmapause region and at altitudes <5,000 km. Multipath and diffuse MR-WM echoes were observed at all latitudes and altitudes <5,000 km.

3. A study of occurrence pattern of WM echoes as a function of both $K_{p,max}$ from past 24 hours and from past 12 hours has shown that WM echoes are observed 20-30% of the time when Kp is moderate (Kp<5). Less than 100 transmissions of program 38 were made at larger values of Kp (>6). Further work is needed to understand the

occurrence pattern of WM echoes during disturbed conditions in the magnetosphere (Kp>6).

In short, WM echoes were observed at all latitudes in the magnetosphere, discrete MR- and SR-WM echoes were more commonly observed at low latitudes, diffuse SR-WM were observed at high latitudes, and diffuse MR-WM echoes were observed at all latitudes, and the geomagnetic conditions were moderate (Kp<5).

The occurrence pattern of WM echoes during selected geomagnetically quiet (Aug 17-Aug 23; Nov 30-Dec 12) and disturbed periods (Aug 24-Sep 24) in Aug-Dec 2005 was studied.

1. The variation of solar activity and geomagnetic activity for the selected quiet and disturbed periods is presented.

2. Electron densities at the satellite location during both quiet and disturbed periods using the lower cut off of MR-WM echoes were calculated. Electron densities vary from 200 el/cc to 2400 el/cc during both quiet and disturbed periods.

3. The plasmapause locations as calculated using $K_{p,amx}$ from past 24 hours and f_{uh} from dynamic spectra indicated that the plasmasphere expands during quiet periods and contracts during disturbed days.

4. TEC measurements during a quiet day (Dec 08, 2005) and when there was a geomagnetic storm (Sep 11, 2005) were presented. These measurements suggest that the low electron density is low ($0.5 * 10^{11}$) at altitudes <800 km during quiet days and the electron density is enhanced by 2 times at 100-400 km altitude during the disturbed day.

5. Occurrence patterns of WM echoes during case study periods is studied. According to both Kp and Dst: a) discrete SR-WM echoes were observed >30% of the time during quiet periods and <10% of the time during disturbed periods, b) diffuse SR-WM echoes were observed 15-20% of the time during both quiet and disturbed periods

and 9% during moderate geomagnetic conditions, c) discrete MR-WM echoes were observed <4% of the time during quiet periods and > 19% of the time during disturbed periods, d) diffuse MR-WM echoes were observed ≈10-20% during quiet periods and ≈10-24% of the time during disturbed periods.

We believe that the irregularities present at altitudes greater than 1,000 km during quiet periods ($f_{lh,max}$ altitude) affect frequencies below $f_{lh,max}$ and above $f_{lh,max}$ differently, thereby significantly affecting MR more than SR-WM echoes. It is, however, interesting that the probability of discrete MR-WM has increased ~5 times from quiet to disturbed periods. These occurrence patterns of WM echoes also suggest that geomagnetic storms lead to significant enhancements in density structures (FAIs) at altitudes lower than 1000 km, thereby affecting primarily the propagation of SR-WM echoes that are reflected at ~90 km but not that of MR-WM echoes because they are reflected at altitudes >1,000 km.

4.2 Recommendations for future work

At low altitudes, IMAGE has observed VLF ground transmitter signals, with a few hundred Hz bandwidth and hundreds of kilowatts of transmitted power, on almost every RPI plasmagram. These observations can be used to detect small scale irregularities (10 m - 1 km). In the presence of small scale FAI, the VLF signals are forward scattered. The scattered waves containing a range of wave normals lead to a spectrally broadened (Δf~1-2 kHz) signal on a moving satellite [Bell et al., 1983]. These spectrally broadened signals can be used to study the length scales of FAI and density enhancements.

Lightning stroke and wave particle interactions at the equator are the known sources of natural WM waves in space. These waves generated in space remain trapped through the reflection process in the magnetosphere and they are either amplified or damped by their interaction processes with energetic particles. The study of WM echoes reflection, refraction and scattering processes as a function of geomagnetic activity helps in a better understanding of naturally occurring WM waves.

A comparison of measured frequency versus time delay dispersion of WM echoes with

that calculated from ray tracing analysis can be used to determine electron density, ion composition, location of FAI, length scales of FAI, and minimum density enhancements of FAI required for scattering to take place [Sonwalkar et al., 2004, Sonwalkar et al., 2006]. The variation of the parameters discussed above can be studied using WM echoes observed on IMAGE during both quiet and disturbed periods.

We see a relation between VLF activity and geomagnetic activity, but further work is needed to establish the relation between VLF activity and geomagnetic activity, VLF activity and the echoing process.

The work presented here will help design a future WM sounder. The RPI instrument on IMAGE is designed to use conventional radio sounding techniques that use free space R-X and L-O mode waves to perform remote sensing measurements of N_e at higher altitudes in the magnetosphere. WM sounding is possible at the lower end of the nominal operating frequency range, 3 kHz - 3 MHz of RPI [Sonwalkar et al., 2001]. IMAGE has an apogee of $8R_E$ and, therefore, not many measurements at lower altitudes were made since IMAGE spends only about 1 hr in the low altitude region. We believe that WM echoes are not detectable by RPI at higher altitudes because of the low signal strength. These constraints could be overcome when active WM experiments are planned, on a low altitude satellite for measurements at low altitudes and on a high altitude satellite with powerful transmitter signals for high altitude measurements. These experiments will help in a better understanding of the electron density, density irregularities, and ion composition variations in the low altitude region (<5,000 km) of the magnetosphere during both quiet and disturbed periods. These experiments will also result in a new understanding of the physics of whistler mode propagation, reflection and scattering in near-Earth space and determine its implications for the interpretation of naturally occurring WM waves.

References

[Bell et al., 1983] Bell, T. F., H. G. James, U. S. Inan, and J. P. Katsufrakis, The apparent spectral broadening of VLF transmitter signals during transionospheric propagation, J. Geophys. Res., 88, 4813, 1983.

[Benson et al., 2003] Benson, R. F., V. A. Osherovich, J. Fainberg, and B. W. Reinisch, Classification of IMAGE/RPI-stimulated plasma resonances for the accurate determination of magnetospheric electron density and magnetic field values, J. Geophys. Res., 108(A5), 1207, doi:10.1029/2002JA009589, 2003.

[Benson et al., 2006] Benson, R. F., P. A. Webb, J. L. Green, D. L. Carpenter, V. S. Sonwalkar, H. G. James, and B. W. Reinisch, Active Wave Experiments in Space Plasmas: The Z Mode, Lect. Notes Phys. , Springer-Verlag, Berlin Heidelberg, 687, 335, 2006.

[Carpenter et a., 1966] Carpenter D L. Whistler studies of the plasmapause in the magnetosphere. 1. Temporal variations in the position of the knee and some evidence on plasma motions near the knee. J. Geophys. Res. 71:693-709, 1966.

[Carpenter and Anderson 1992] Carpenter, D. L. and R. R. Anderson, An ISEE/Whistler model of equatorial electron density in the magnetosphere, J. Geophys. Res., 97, 1097, 1992.

[Carpenter et a., 1997] Carpenter, D. L., V. S. Sonwalkar, R. A. Helliwell, M. Walt, U. S. Inan, M. Ikeda, and D. L. Caudle, Probing properties of the magnetospheric hot plasma distribution by whistler mode wave injection at multiple frequencies: Evidence of spatial as well as temporal wave growth, J. Geophys. Res., 102(A7), 14,355-14,362, 1997.

[Carpenter et al., 2003] Carpenter, D. L., T. F. Bell, U. S. Inan, R. F. Benson, V. S. Sonwalkar, B. W. Reinisch, and D. L. Gallagher: Z-mode sounding within propagation "cavities" and other inner magnetospheric regions by the RPI instrument on the IMAGE satellite, J. Geophys. Res. 108, 1421, 2003.

[Carpenter et al., 2007] Carpenter, D. L., T. F. Bell, D. Chen, D. Ng, C. Baran, B. W. Reinisch, and I. Galkin, Proton cyclotron echoes and a new resonance observed by the Radio Plasma Imager instrument on the IMAGE satellite, J. Geophys. Res., 112, A08208, doi:10.1029/2006JA012139, 2007.

[Coordinated Data Analysis Web database] Date retrieved: September, 2006
$http://cdaweb.gsfc.nasa.gov/cdaweb/istp_public/$

[Helliwell et al., 1965] Helliwell, R. A., Whistlers and Related Ionospheric Phenomena, Stanford University Press, Stanford, California, 1965.

[Helliwell, 1988] Helliwell, R. A., VLF wave stimulation experiments in the magnetosphere from Siple Station, Antarctica, Reviews of Geophysics, 26, 551, 1988.

[James, 1972] James, H. G., Refraction of whistler-mode waves by large-scale gradients in the middle latitude ionosphere, Ann. Geophys., 28(2), 301- 309, 1972.

[Kelley 1989] Kelley, M. C., The Earth's Ionosphere, Academic Press, Inc., 1989.

[Kletzing et al., 1998] Kletzing, C. A., F. S. Mozer, and R. B. Torbert, Electron temperature and density at high latitude, J. Geophys. Res., 103, 14837, 1998.

[Osherovich et al., 2007] Osherovich, V. A., R. F. Benson, J. Fainberg, J. L. Green, L. Garcia, S. Boardsen, N. Tsyganenko, and B. W. Reinisch, Enhanced high-altitude polar cap plasma and magnetic field values in response to the interplanetary magnetic cloud that caused the great storm of 31 March 2001: A case study for a new magnetospheric index, J. Geophys. Res., 112, A06247, doi:10.1029/2006JA012105,2007.

[Persoon et al., 1983] Persoon, A. M., D. A. Gurnett, and S. D. Shawhan, Polar cap electron densities from DE 1 plasma wave observations, J. Geophys. Res., 88, 10123, 1983.

[Reinisch et al., 2000] Reinisch, B. W., D. M. Haines, K. Bibl, G. Cheney, I. A. Galkin, X. Huang, S. H. Myers, G. S. Sales, R. F. Benson, S. F. Fung, J. L. Green, W. W. L. Taylor, J. L. Bougeret, R. Manning, N. Meyer-Vernet, M. Moncuquet, D. L. Carpenter, D. L. Gallagher, and P. H. Reiff, "The Radio Plasma Imager Investigation on the IMAGE Spacecraft," Space Science Reviews, 91, pp. 319-359, 2000.

[Schunk and Nagy, 2000] Schunk, R. W., and A. F. Nagy, Ionosphere:, Physics, Plasma Physics, and Chemistry, Cambridge University Press, 2000.

[Sojka et al., 2000] Sojka, J. J., L. Zhu, M. David, and R. W. Schunk, Modeling the evolution of meso-scale ionospheric irregularities at high latitudes, Geophys. Res. Lett., 27, 3595, 2000.

[Sonwalkar et al., 1984] Sonwalkar, V. S., T. F. Bell, R. A. Helliwell, and U. S. Inan, Direct multiple path propagation: A fundamental property of nonducted VLF waves in the magnetosphere, J. Geophys. Res., 89, 2823, 1984.

[Sonwalkar et al., 1997] Sonwalkar, V. S., D. L. Carpenter, R. A. Helliwell, M. Walt, U. S. Inan, D. L. Caudle, and M. Ikeda, Properties of the magnetospheric hot plasma distribution deduced from whistler mode wave injection at 2400 Hz: Ground-based detection of azimuthal structure in magnetospheric hot plasmas, J. Geophys. Res., 102(A7), 14,363-14,380, 1997.

[Sonwalkar and Harikumar, 2000] Sonwalkar, V. S., and J. Harikumar, An explanation of ground observations of auroral hiss: Role of density depletions and meter-scale irregularities, J. Geophys. Res., 105, 18,867,2000.

[Sonwalkar et al., 2001] Sonwalkar, V. S., X. Chen, J. Harikumar, D. L. Carpenter, and T. F. Bell, Whistler-mode wave-injection experiments in the plasmasphere with a radio sounder, J. Atmos. Solar Terr. Phys., Vol. 63, issue 11, 2001.

[Sonwalkar et al., 2004] Sonwalkar, V. S., D.L. Carpenter, T. F. Bell, M.A. Spasojevic, U. S. Inan, J. Li, X. Chen, A. Venkatasubramanian, J. Harikumar, R. F. Benson, W. W. L. Taylor, and B. W. Reinisch, Diagnostics of magnetospheric electron density and irregularities at altitudes ¡5000km using whistler and Z mode echoes from radio sounding on the IMAGE satellite, J. Geophys. Res., 109, A11212, 2004.

[Sonwalkar, 2006] Sonwalkar, V. S., The Influence of Plasma Density Irregularities on Whistler-Mode Wave Propagation, Lect. Notes Phys., Springer-Verlag, Berlin Heidelberg, 687, 141-191, 2006.

[Sonwalkar et al., 2006] Sonwalkar, V. S., D. L. Carpenter, R. Proddaturi, A. Reddy, B. Reinisch, Observations of Magnetospherically Reflected (MR) Whistler Mode (WM) Echoes Observed by Radio Plasma Imager (RPI) on the IMAGE Satellite: Diagnostics of Electron Density and Ion Composition, AGU 2006 Fall Meeting, abstract SM11B-0323, 11-15 December, San Francisco, California, USA, 2006.

[Sonwalkar et al., 2007] Sonwalkar, V. S., A. Reddy, R. V. Proddaturi, D. L. Carpenter, B. W. Reinisch, Whistler- and Z-mode Echoes Observed on IMAGE: Relation to Geomagnetic Activity, General Assembly of International Union of Radio Science (URSI), 22-26 July, Ottawa, ON, Canada, 2007.

[Sonwalkar, 2007] Sonwalkar, V. S., Observations, Simulations, and Modeling of Space Plasma Waves: A Perspective on Space Weather, 6th International Workshop, Data

Analysis in Astronomy, Modelling and Simulation in Science, 15 - 22 April, Erice, Italy, 2007.

[Storey, 1953] Storey, L. R. O, An investigation of whistling atmospherics, Phil. Trans. Roy. Soc. Lond., 246, 113-141, 1953.

[Tu et al., 2007] Tu, J.-N., M. Dhar, P. Song, B. W. Reinisch, J. L. Green, R. F. Benson, and A. J. Coster, Extreme polar cap density enhancements along magnetic field lines during an intense geomagnetic storm, J. Geophys. Res., 112, A05201, doi:10.1029/2006JA012034, 2007.